Paleointensities of phonolitic obsidian: Influence of emplacement rotations and devitrification

A. Ferk,[1,2] R. Leonhardt,[1] F. W. von Aulock,[2] K.-U. Hess,[2] and D. B. Dingwell[2]

Received 28 March 2011; revised 17 October 2011; accepted 19 October 2011; published 31 December 2011.

[1] A paleomagnetic study on phonolitic obsidian from six sites in Tenerife, Spain is presented. Two sites are located at the 750 ka El Pasajiron at the southern wall of Las Cañadas Caldera. Four sites correspond to the 115 ± 17 BCE Montaña Blanca Complex. Paleointensity determinations are performed with a modified Thellier technique using checks for alteration and domain state. Additionally, the anisotropy of the thermoremanence and the magnetic cooling rate dependency of each specimen are measured. It was not possible to obtain good quality paleointensity data for El Pasajiron. Thermal alteration was observed in most measurements. Systematic changes in rock magnetic properties and paleointensities within the profile of one site also suggest the presence of a chemical remanence (CRM) which was probably acquired during devitrifiction of the upper part of the flow. This CRM cannot be seen in the Arai plots themselves but only by comparison of data from different samples. This underlines the importance of sampling only fresh glassy looking obsidians and not devitrified ones. Paleointensity determinations at Montaña Blanca are of very good quality leading to an high success rate of 82%. Samples at one site show acquisition of TRM during emplacement rotations. However, it could be shown that paleointensity data of rotated samples are reliable if the remanence carriers are in the single domain range. An ATRM (anisotropy tensor of thermoremanent magnetization) and cooling rate corrected paleointensity of 48.4 ± 2.1 μT and a VDM of 9.64 ± 0.42 * 10^{22}Am^2 were determined which are in very good agreement with other data from Spain and Morocco and to various geomagnetic field models.

Citation: Ferk, A., R. Leonhardt, F. W. von Aulock, K.-U. Hess, and D. B. Dingwell (2011), Paleointensities of phonolitic obsidian: Influence of emplacement rotations and devitrification, *J. Geophys. Res.*, *116*, B12113, doi:10.1029/2011JB008397.

1. Introduction

[2] Several studies [*Pick and Tauxe*, 1993; *Selkin and Tauxe*, 2000; *Leonhardt et al.*, 2006; *Ferk et al.*, 2010] suggest that volcanic glass is an excellent recording material for paleointensity studies. Use of volcanic glass enables several problems that cause failure or bias in paleointensity data to be overcome: Magnetic domain state bias affecting the different remanence acquisition processes in nature and in the laboratory [*Leonhardt et al.*, 2004b] can be largely excluded as the remanence carriers are either single-domain (SD) or small pseudo-single-domain (PSD) grains [*Geissman et al.*, 1983; *Juárez et al.*, 1998; *Smirnov and Tarduno*, 2003; *Leonhardt et al.*, 2006]. Further, some volcanic glasses have a pristine character with seemingly low alterations in geological time and in laboratory experiments [*Pick and Tauxe*, 1993]. Last, but not least their cooling histories are either comparable to those in the laboratory [*Bowles et al.*, 2005] or a correction for cooling rate dependency [*Fox and Aitken*, 1980; *Halgedahl et al.*, 1980] is possible by determining the natural cooling rates of the samples [*Leonhardt et al.*, 2006; *Ferk et al.*, 2010] via relaxation geospeedometry [*Wilding et al.*, 1995, 1996a, 1996b; *Gottsmann and Dingwell*, 2001a, 2001b; *Gottsmann et al.*, 2004; *Potuzak et al.*, 2008; *Nichols et al.*, 2009]. Thus, for SD particles that acquire weaker thermoremanent magnetizations (TRM) when cooled faster, paleointensity overestimates of more than 20% can be corrected for.

[3] Problems can be encountered, however, when working with volcanic glass. *Smirnov and Tarduno* [2003] demonstrated that laboratory alteration causes bias in paleointensity experiments if the glass transition occurs below the blocking temperature of the remanence. Laboratory heating steps to temperatures above this transition can lead to alterations of magnetic minerals that would not necessarily be detected by alteration checks. Fortunately, determination of natural cooling rates via geospeedometry also yields the glass transition temperature T_g and thus by its comparison with blocking or Curie temperatures such alteration can often be ruled out.

[4] In this study two other problems are examined: One is the devitrification of volcanic glass. The glass transition is a

[1]Conrad Observatory, Central Institute for Meteorology and Geodynamics, Vienna, Austria.
[2]Department of Earth and Environmental Sciences, Ludwig-Maximilians-Universität, Munich, Germany.

0148-0227/11/2011JB008397

Figure 1. Obsidian block in Iceland that was squeezed during emplacement.

kinetic boundary below which the time required for melt relaxation increases greatly. Nevertheless, in geologic times sub T_g relaxation may become important. Hydration can additionally speed up crystallization. This might lead to magnetomineralogical changes and contemporaneous new remanence acquisition, which biases paleomagnetic experiments. The second problem is that during emplacement of obsidians significant strain, rotation and compression occur. Obsidian flows are often blocky lava flows and the blocks are often not *in situ*. Additionally, some obsidians have been compressed during their emplacement (e.g., Figure 1). Care must be taken to ensure that paleointensities determined on samples from such rotated and/or squeezed blocks are reliable.

[5] Here we present data from a 750 ka old partially devitrified obsidian at the Caldera Wall of Las Cañadas Caldera, Tenerife and results from a site within the Caldera, originating from the ~2 ka BP Montaña Blanca eruption, that shows emplacement rotation/compression and block break-up while cooling. Further we provide high quality anisotropy and cooling rate corrected data for 115 ± 17 BCE at Tenerife.

2. Geology and Sampling

[6] Tenerife is the largest of the Canary Islands. Upper Miocene and Lower Pliocene basaltic series are found in the Anaga, Teno and Rocque del Conde massifs [*Ancochea et al.*, 1990]. Later volcanic activity was concentrated on Las Cañadas central volcano, the NW-SE trending rift of Santiago del Teide and the Cordillera Dorsal, a SW-NE trending ridge linking Las Cañadas and the Anaga. The upper part of Las Cañadas volcano was destroyed and forms the so-called Las Cañadas Caldera, which was formed during different vertical and lateral collapses [e.g., *Marti et al.*, 1994]. At its southern part the caldera wall is visible and reaches up to 500 m above the rest of the edifice. Lavas from the Pico Teide (3718 m) -Pico Viejo formation filled parts of the caldera and were also emplaced along the northern slopes of the island (Figure 2).

[7] Samples were obtained using a water-cooled electrically driven drill on a field trip to Tenerife in September 2007. Whenever possible, sampling took place at sites where a gradient in cooling rates was suspected and where pristine clear glass with low crystal content was found (Figure 2). Pictures of the different sites can be seen in Figure 3. Two sites were sampled at El Pasajiron (EPJ, N28°13′24″, W016°36′14″; all coordinates WGS84) at the southern caldera wall just to the east of Guajara, the highest point of the wall. A K-Ar date of El Pasajiron gives a date of 800 ka [*Marti et al.*, 1994]. However, according to its stratigraphic position and the age of other units of the same eruption, a younger age of ~750 ka is more probable. An age within the Bruhnes chron, i.e. the last 780 ka, is also supported by our normal directional data (section 5). At site EPJ1 we took four samples in a vertical profile of about 60 cm, and at site EPJ2 eight samples in another vertical profile of about 1.3 m height. Here, the uppermost samples EPJ2-1 to EPJ2-3 are in a fully devitrified part while EPJ2-4 to EPJ2-6 are in the partly devitrified middle of the outcrop and EPJ2-7 and EPJ2-8 are in the lowermost part consisting of fresh obsidian. The other four sites are at the Montaña Blanca (MB) complex, which is a flank vent complex at the eastern flank of Teide comprising MB and Montaña Rajada (MR) and resulting from the only well known post-caldera explosive eruption at 2065 ± 17 BP (i.e. 115 ± 17 BCE) [*Ablay et al.*, 1995]. This age is a C14 age in calibrated years before present, with 95% confidence level and was calculated as weighted average and weighted standard deviation of the three C14 age determinations done by *Ablay et al.* [1995] using 1/standard deviation as weighting factor. The MB eruption involved effusion of lava and deposition of thick pyroclastic fallouts during a subplininan phase. Site MBT1 (MB Tabonal Negro 1, N28°15′29″, W016°36′10″) is within El Tabonal Negro. This fresh, blocky phonolitic lava flow represents the beginning of the eruption. As the partly overlying pumice is not baked or oxidized, perhaps only months may have separated these two phases of the eruption [*Ablay et al.*, 1995]. Seven samples were taken as a horizontal profile on each of two big ~2 m wide blocks that seemed to have broken apart in the middle. Samples were taken in more or less regular intervals of 10 to 20 cm within the black, glassy layers which are alternated with brown, more devitrified layers. The different blocks may represent parts of one original obsidian block that, still warm, was quenched from both sides and broke apart. The outsides of the two blocks are covered with clinker of up to 10 cm. Site MBU1 (Upper MB 1; 5 samples in a vertical profile, N28°16′7″, W016°36′49″) is an about 80 cm thick *in situ* lava flow at the top of MB. This lava flow belongs to the same phase of the eruption as El Tabonal

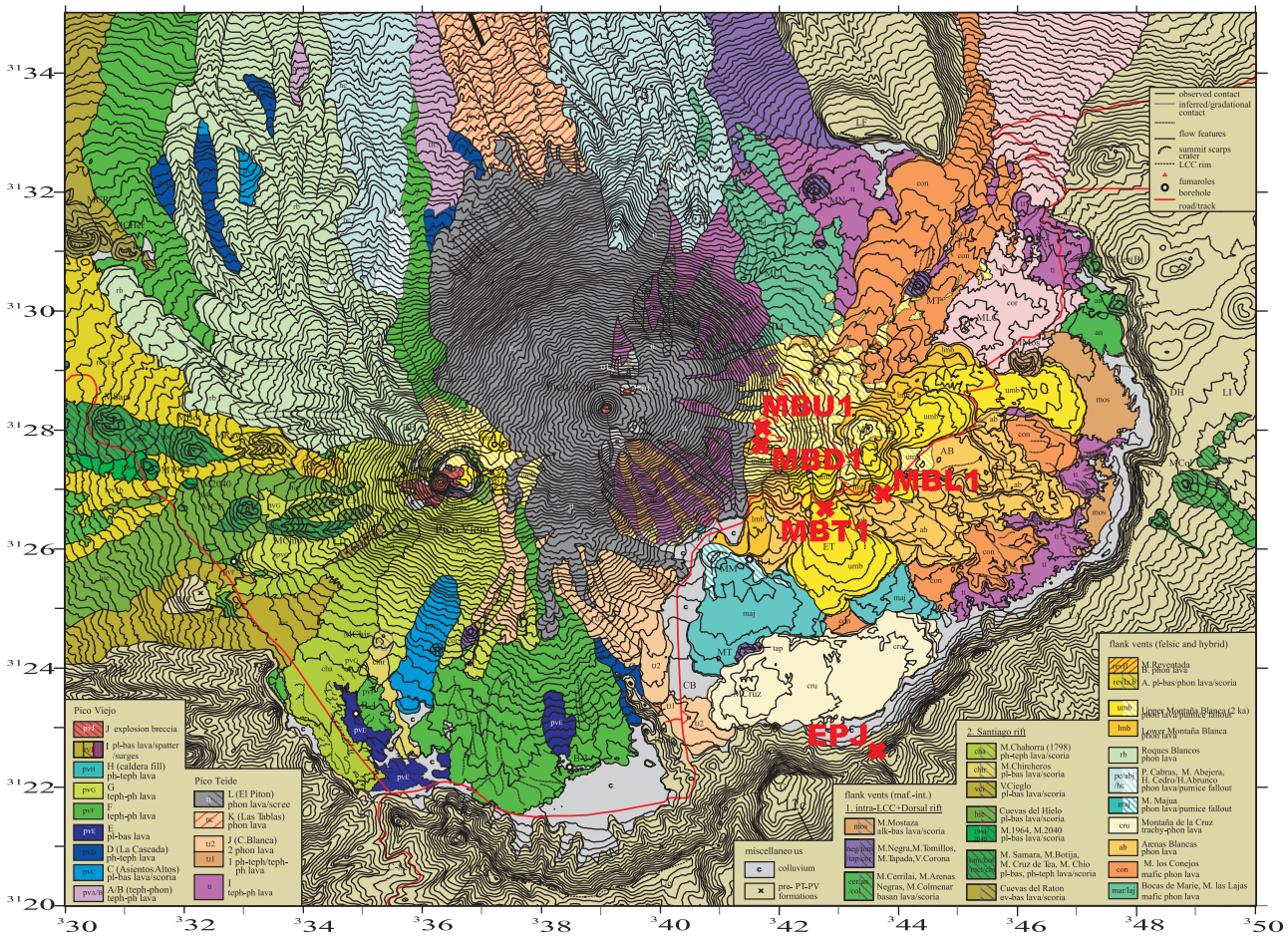

Figure 2. Geologic map of Las Cañadas Caldera (reprinted from *Ablay and Marti* [2000], copyright 2000, with permission from Elsevier) including the sampling sites (red crosses); coordinates refer to 2 km squares of the Spanish national grid (UTM projection, sector 28 North).

Negro and is one of the few places at the pumice covered hill of MB, where blocks of lava crop out. Samples from the same site have been taken previously by *Gottsmann and Dingwell* [2001a] (name of sampling site in that publication: MB5) for relaxation geospeedometry. The two other sites are from the latter lava flow and dome effusion which was erupted subsequent to deposition of a pumice layer separating those flows from the lower flow. The nine samples of MBD1 (MB Dome 1, N28°15′57″, W016°36′50″) were taken at the western side of the uppermost dome structure at the MB fissure. The material is very homogeneous but less glassy. The samples span about 3 m in height. Site MBL1 (MB Lavas in block 1, N28°15′37″, W016°35′34″) lies just a few meters south of the road TF-21 and belongs to a blocky lava flow that was erupted from MR during the third phase of the whole eruption. Our 7 samples represent 1.5 m of the 3 m high block and range from very devitrified looking whitish material (MBL1-1 to MBL1-5) to a black and pristine glass layer at the bottom of the block (MBL1-6, MBL1-7).

[8] From each of the samples we took some miniature cores of varying diameter (5 mm to 8 mm), that were subjected to a set of calorimeteric investigations, rock magnetic measurements at room and high temperature, paleodirectional analyzes and paleointensity experiments including determination of the anisotropy of thermoremanence and the dependence on cooling rate.

3. Relaxation Geospeedometry

[9] Relaxation geospeedometry, i.e. measurements of the heat capacity at constant pressure c_p, can be used to determine both the glass transition temperature T_g and the natural cooling rate. By passing through the glass transition, the melt changes from liquid-like viscous to solid-like brittle behavior; it passes from metastable equilibrium to disequilibrium. T_g does depend not only on the composition of the melt, but also on the quench rate. A record of the quench rate at the glass transition is frozen in the glass structure and can be accessed by reheating the sample together with parallel measurement of a structure dependent physical property such as heat capacity c_p. The concept of fictive temperature T_f is used to simplify the understanding of structural relaxation at the glass transition [*Tool*, 1946]. T_f expresses the temperature at which the temperature-dependent property of the glass is equal to that of the supercooled liquid. Above the glass transition the relaxation time τ to achieve equilibrium is short and thus the melt is in equilibrium: T_f equals the actual temperature T. At lower temperatures, τ increases and the melt departs from equilibrium where

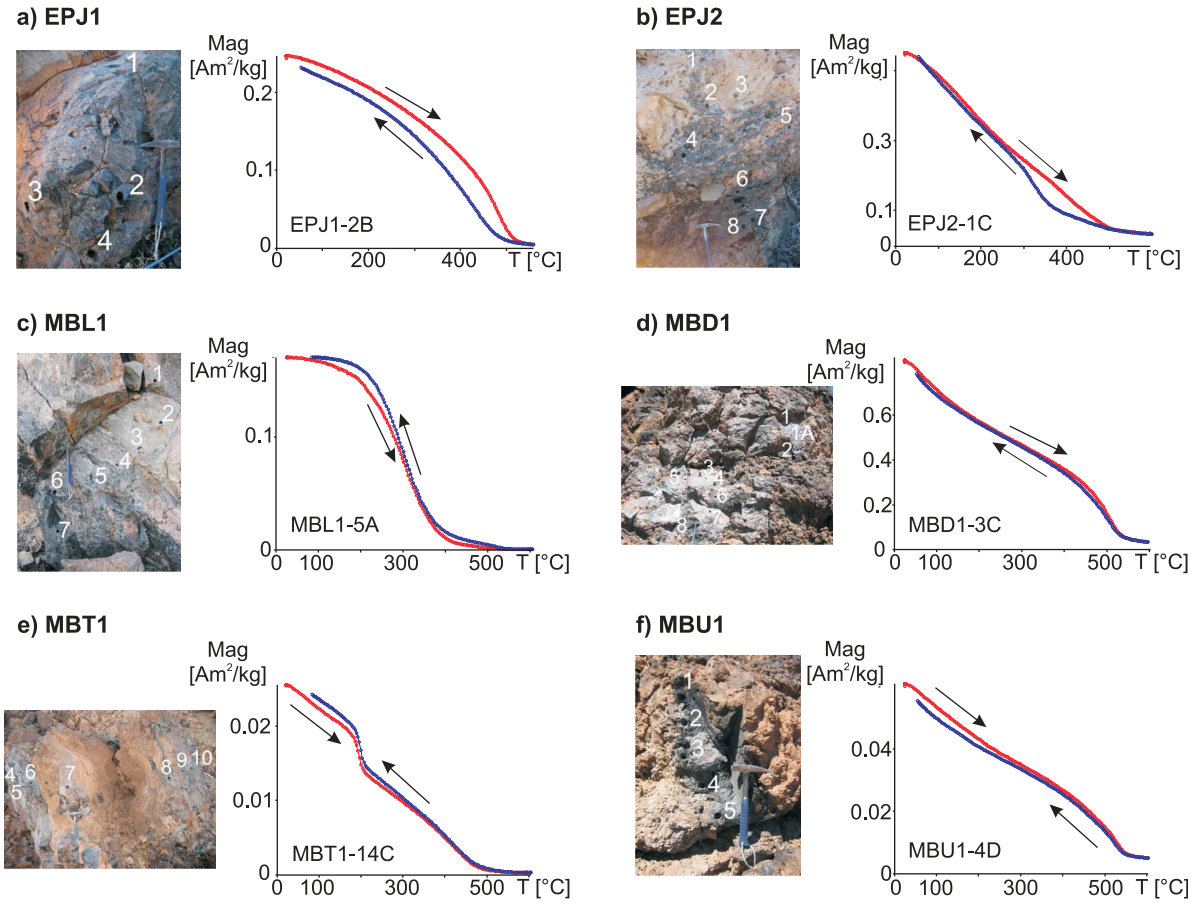

Figure 3. Pictures of the six different sites with sample positions indicated and respective thermomagnetic curves for each site.

$T_f > T$. At this point the glass transition is entered and persists through a certain temperature interval. Below that interval the glass structure is frozen in and T_f is constant. The temperature at which the structure is frozen in depends on cooling rate: during faster cooling adjustment to new equilibrium is more restricted and hence, the structure is frozen in earlier. When reheating the sample, T_f depends both on the heating and on the previous cooling rate. T_f can be monitored by measuring c_p, first derivative of enthalpy H. Within the glass transition region c_p shows a peak during heating, which may be operationally defined as T_g (e.g., Figure 4). As the heating curve depends on the previous cooling, an initial heating curve is modeled with four kinetic parameters that are obtained in successive heating/cooling runs with known rates. This enables a calculation of the natural cooling rate (respective temperature range: [T_g − 200°C, T_g + 50°C]). Following the approach by *Wilding et al.* [1995] the Tool-Narayanaswamy [*Narayanaswamy*, 1971, 1988] equation for relaxation and the Debolt equation [*Debolt et al.*, 1976] for fictive temperature were used for this modeling.

[10] Specimens for relaxation geospeedometry were prepared by drilling cylinders of 6 mm diameter and cutting these into disks of approximately 1 mm. Then they were polished down to 55 ± 2 mg, that is approximately the weight of the corundum standard (55 mg) which was used for quantitative measurements of c_p. The samples were dried for half an hour at 105°C. As far as possible no parts with visible alteration, devitrification or crystals were used. The measurements were done on a Netzsch Differential Scanning Calorimeter (DSC) 404 F1 Pegasus. The sample chamber was evacuated and flushed three times with high quality

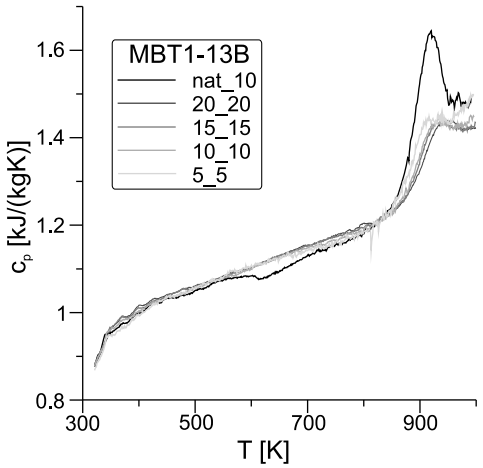

Figure 4. C_p curves for MBT1-13B as measured during heating. The different cooling/heating cycles are labeled: For example, nat_10 indicates previous, natural, cooling and then heating with a rate of 10 K/min.

Table 1. Relaxation Geospeedometry[a]

Sample	T_g (±6°C)	Natural Cooling Rate (K/min)
	El Pasajiorn	
EPJ1-2B	560	0.0005
EPJ1-3B	609	0.0025
EPJ2-4B	669	0.0006
EPJ2-7B	682	0.0001
EPJ2-8B	682	0.004
	Montaña Blanca	
MBD1-2B	625	0.02
MBD1-3C	624	0.07
MBD1-4B	627	0.38
MBD1-5B	669	0.0004
MBD1-6B	624	0.02
MBD1-7C	624	0.02
MBD1-8B	634	0.01
MBT1-1B	617	10
MBT1-2C	661	0.8
MBT1-3C	621	0.1
MBT1-4B	647	0.5
MBT1-5C	615	0.05
MBT1-6B	621	0.1
MBT1-7C	615	$2*10^{-6}$
MBT1-8B	636	0.05
MBT1-9	618	0.6
MBT1-10C	601	0.24
MBT1-11B	624	5
MBT1-12B	624	6
MBT1-13B	646	10
MBT1-14B	626	12
MBU1-1C	633	0.05
MBU1-3B	634	0.03
MBU1-4B	634	0.001
MBU1-5B	633	0.02

[a]Glass transition temperatures T_g (peak of the first (natural) run with 10 K/min heating rate) and natural cooling rates of indicated samples.

Argon 5.0 (99.999% pureness; concentrations: $O_2 \leq 2$ ppm, $H_2O \leq 3$ ppm) before the insertion of the sample. During the measurement a constant flow of 25 ml/min Argon 5.0 prevented bulk oxidation and ensured constant atmospheric conditions. The sample was heated and cooled in the DSC with successive rates of 10 (only heated), 20 (cooled/heated), 15 (cooled/heated), 10 (cooled/heated) and 5 (cooled/heated) K/min (respective temperature range for all runs: [T_g – 200°C, T_g + 50°C]). T_g is determined as the peak of the first (natural) run with 10 K/min heating rate. The four later runs (20, 15, 10 and 5 K/min) which are no longer influenced by natural cooling allow an estimation of the sample specific parameters. These can then be used to fit the first run, by adapting the previous, i.e. natural, cooling rate.

[11] Relaxation geospeedometry was done on samples from all sites (Table 1). The best data was obtained for MBT1. Only MBT1-7C is an outlier with an extremely slow cooling rate of 2.0 * 10^{-6} K/min (10.5 K/year). For MBT1-1B the result of the measurement is promising, but its initial c_p curve is disturbed by reactions or phase transitions within the sample that are not yet understood. Therefore, influences on cooling rate estimation can not be ruled out. T_g is between 601°C for MBT1-10C and 661°C for MBT1-2C. At the outer rims of the two blocks high cooling rates of 10 to 12 K/min are observed, while in the middle where the two blocks lie next to each other low cooling rates of about 0.1 K/min are seen. This supports our field hypothesis that we are dealing with one block that has broken in two parts. The trend of the cooling rates in the interior of this whole block is asymmetrical to one side as the gradient of cooling rates is much higher on the left side. At MBU1 all samples show a large change in c_p of the supercooled liquid for the slow cooling cycle with 5 K/min at the end of the experiment. Nonetheless, it was possible to determine constant T_g of 633–634°C and the cooling rates range between 0.001 K/min and 0.05 K/min, which are in the same range as the data by *Gottsmann and Dingwell* [2001b]. Natural cooling rates of MBD1 range between 0.0004 K/min (0.58 K/day) and 0.38 K/min without any apparent trend and the T_g of these samples are between 624 and 669°C. Due to the low glass content of the MBL1 samples, no peak in c_p curves is found and thus, no results could be obtained for MBL1. Results for the glassy samples of the much older El Pasajiron sites are very good with the exception of EPJ1-1 and EPJ2-4. EPJ1-1 has too high a crystallinity to show a peak at T_g and c_p of EPJ2-4 changed after the first heating cycle. Natural cooling rates range between 0.0005 K/min (0.72 K/day) and 0.0025 K/min (0.15 K/h)for EPJ1 and between 0.0001 K/min (0.14 K/day) and 0.004 K/min (0.24 K/h) for EPJ2. Thus, cooling was considerably slower than for most MB samples. This could be due to the fact that EPJ is a welded deposition with a high deposition rate and therefore, a thick layer that took longer to cool down. T_g for EPJ1 samples is between 560 and 609°C and for EPJ2 samples between 669 and 682°C.

4. Magnetic Mineralogy and Domain State

[12] Rock magnetic measurements were performed to analyze magnetic mineralogy and domain state. Isothermal remanent magnetization (IRM) acquisition, isothermal backfield curves, hysteresis loops at room temperature and thermomagnetic curves were measured on a Variable Field Translation Balance (VFTB) using 5 mm diameter miniature cores. At least one sample of each site was heated in air stepwise to 420°C, 470°C, 520°C and, when necessary to reach the Curie temperature T_C, up to 560°C and 600°C. Between each of these steps additional backfield and hysteresis measurements at room temperature were done to test the thermal stability of the samples. Rock magnetic data of all samples can be found in Table S1 in the auxiliary material.[1] Ore microscopy using oil objectives with magnifications of 50 and 125 was done on at least one sample per site that had previously been polished down to 1 μm.

[13] Thermomagnetic curves (Figure 3) yield T_Cs for EPJ1 of 500°C to 520°C and for EPJ2 of 450°C to 530°C. The thermomagnetic curves of EPJ2-1C and EPJ2-2D decline continuously while those of all other samples drop relatively sharply at T_C. MBL1 samples lose most of their magnetization already at low T_Cs of 200°C to 350°C, but also have a small contribution of a second higher T_C at 400°C to 520°C. Specimens from MBD1 have a high T_C about 530°C and a low T_C at 200°C to 390°C which, however, is not always very obvious. Three different T_Cs are observed in samples from MBT, though not each in every sample: One low T_C

[1]Auxiliary materials are available in the HTML. doi:10.1029/2011JB008397.

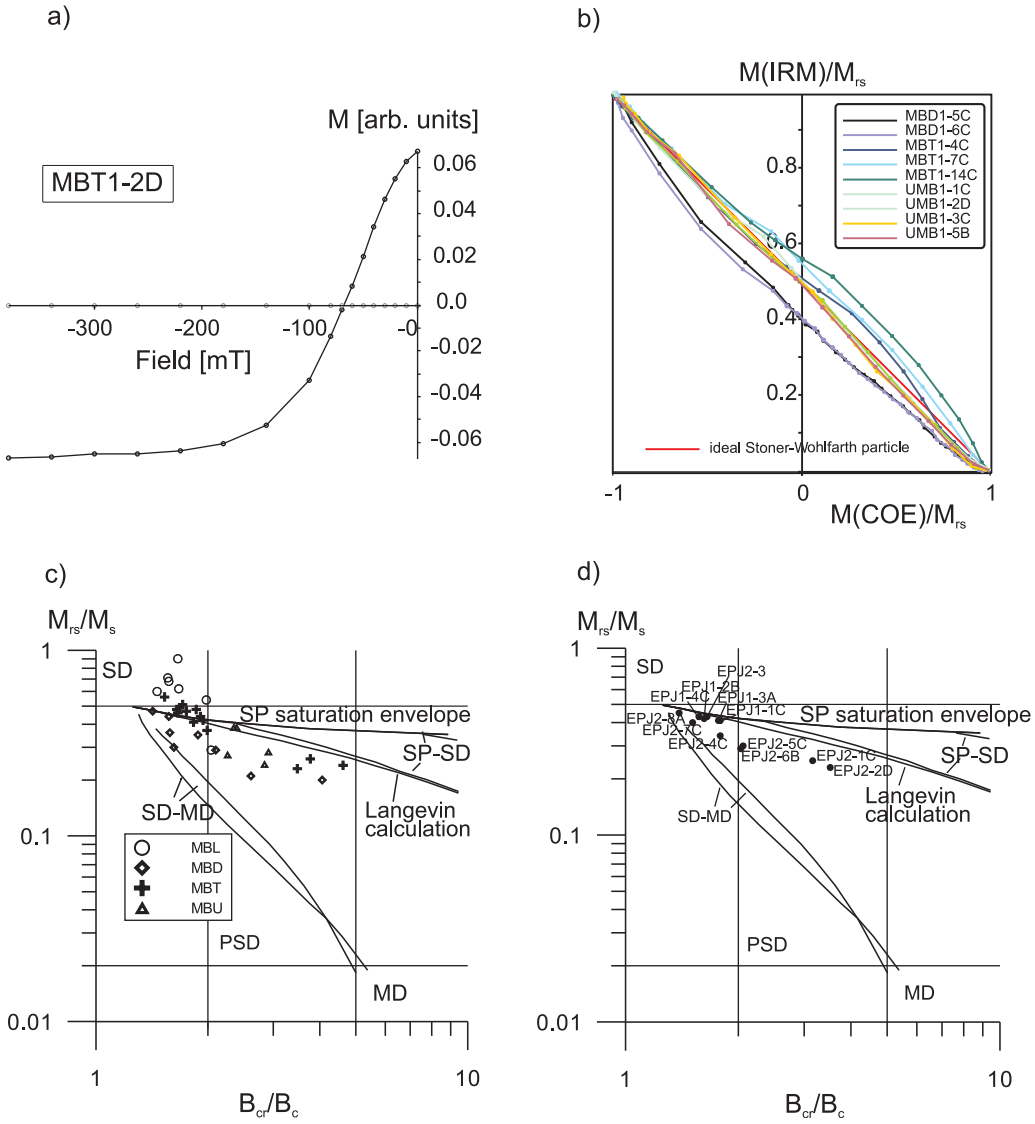

Figure 5. (a) Backfield curve of sample MBT1-2D. (b) Henkel plots [*Henkel*, 1964] of all Montaña Blanca (MB) samples that are in the PSD range of the Day plot. Day plots [*Day et al.*, 1977] with domain state related boundaries and mixing lines by *Dunlop* [2002] of samples from (c) MB and (d) El Pasajiron.

between 200°C and 240°C, one middle between 470°C and 530°C and a high one at 570°C. While the middle T_C is found in every sample, only sample MBT1-7C shows the high T_C and the low T_C is observed in samples MBT1-4C, MBT1-7C, MBT1-11A, MBT1-13A and MBT1-14C. All MBU1 specimens have a high T_C of ~550°C and a second low T_C between 90°C and 240°C, which is not always very prominent.

[14] Taken together, in all cases where T_g could be determined it is well above T_C and no alteration connected to $T_b > T_g$ [*Smirnov and Tarduno*, 2003] should occur during the paleointensity experiments. Further, heating and cooling curves from samples of all sites are almost reversible, at least when not heated far above the upper T_C. This already indicates the absence of any other alteration, which is further supported by hysteresis and backfield measurements conducted together with the stepwise heating: their parameters are almost identical after the different heating steps.

[15] Plotted in a Day plot [*Day et al.*, 1977] with domain state related boundaries and mixing lines by *Dunlop* [2002], single-domain (SD) or at least close to SD behavior is indicated for ~65% of the samples (Figures 5c and 5d). Only 15 of the 47 samples show grain sizes in the pseudo-single-domain (PSD) range for both M_{rs}/M_s and B_{cr}/B_c. At MBL1 only sample MBL1-1 has a too low M_{rs}/M_s value while all the other samples plot clearly within the SD panel. Similar to MBL1-1 also most samples from EPJ1, EPJ2, MBD1 and MBT1 have slightly too low M_{rs}/M_s values, but are still close to SD. The other samples from these sites as well as the samples from MBU1 lie within the PSD panel. A closer look at their position in the Day plot suggests an influence of superparamagnetic (SP) particles [*Tauxe et al.*, 1996]. Further insight into the domain state of the specimens can be gained through Henkel plots [*Henkel*, 1964] (Figure 5b): Here backfield and IRM data, i.e. remanence data, are plotted together. The diagonal of the plot represents ideal

Table 2. Paleodirections[a]

Locality or Site	n/N	D (deg)	I (deg)	k	α_{95} (deg)
El Pasajiorn	8/10	359.7	39.1	65	6.9
EPJ1	3/4	8.6	45.0	258	7.7
EPJ2	5/6	355.1	35.3	90	8.1
Montaña Blanca	17/19	357.4	47.7	125	3.2
MBL1	4/6	356.6	50.1	172	7.0
MBD1	8/8	355.8	47.8	127	4.9
MBU1	5/5	0.3	45.5	92	8.0

[a]Mean directions (D, I) of the different sites and localities together with uncertainty values (k, α_{95}). n/N indicates number of directions used for calculation of mean (n) versus number of directions determined (N).

Stoner-Wohlfarth particles; that is, uniaxial non-interacting single-domain particles [*Wohlfarth*, 1958]. Not only for the samples within or very close to the SD panel, but also for those within the PSD panel the data are very close to the ideal line suggesting a predominant SD character of the remanence-carrying particles.

[16] High B_{cr} values between 65 mT and 135 mT are observed for all samples. Thus, shape anisotropy is indicated. Only samples MBL1-1A, MBL1-2C and MBL1-3C have B_{cr} values as low as 35 mT and, thus, should not show any prominent anisotropy. Further the trend from high B_{cr} values for the nondevitrified samples to lower values for devitrified ones (section 7.2) suggests a connection between devitrification processes and change in B_{cr}, e.g. a shortening of grains with previous uniaxial symmetry.

[17] Unfortunately, it was very difficult to get information from ore microscopy, as the glassy matrix can not be resolved. However, a few grains of slightly larger sizes (mostly between 1 and 3 μm, in some cases up to 15 μm) were found to be distributed evenly about the samples of MB and EPJ. The brightness of these mostly rounded, sometimes elongated minerals changes under polarized light. As ore microscopy was unable to resolve the glassy matrix, magnetic force microscopy was done on some samples. However, even for this method, grain sizes were either too small or ferromagnetic particles too rare within the samples and thus, it was impossible to get any picture of magnetic domains.

[18] As backfield and IRM curves for all sites saturate at low fields (i.e. mostly below 300 mT) (e.g., Figure 5a), low coercive remanence carriers, as for example (titano-) magnetite are probable. For silicic melts *Buddington and Lindsley* [1964] found that titanomagnetites can only be responsible for relatively high T_Cs as no titanomagnetites with high titanium content are usually found within these. In contrast, low T_Cs are due to more titanium-rich hemoilmenites which can coexist in silicic melts together with the titanium-poor titanomagnetites [*Buddington and Lindsley*, 1964]. Although we are dealing with melts of phonolitic composition, this observation fits also to the results of ore microscopy, as hemoilmenites are optically anisotropic and often rounded or needle-shaped. Thus, the data suggest that the main remanence carriers of our samples are low-titanium titanomagnetites that are too small to be resolved using ore microscopy and within or close to the SD range. At MB these titanomagnetites are mostly accompanied by high-titanium hemoilmenites of slightly larger grain sizes: Those grains that were seen to change their brightness under polarized light. These generally contribute only very little to the whole remanence.

5. Paleodirections

[19] Thermal demagnetizations to less than 10% of the NRM were done on at least 4 samples (inch cores) per site using a Schoenstedt furnace in the paleomagnetic laboratory of LMU Munich in Niederlippach. All magnetization measurements were carried out on a Molspin magnetometer. After each measurement of the remaining NRM the susceptibility was measured on a KLT-3 Minikappa bridge to detect alteration. Sometimes relative changes of up to 20% were observed, which were however not seen as continuous changes, but as sudden changes between two measurements, that came back to the original values at later measurements. These were therefore accorded to drifts in the instrument rather than to alteration. For most samples changes of only up to 10% were observed. After determination of the specimens' directions by principle component analysis (PCA) [*Kirschvink*, 1980], the mean direction of each site as well as of each locality (El Pasajiron, Montaña Blanca) were calculated using Fisher statistics [*Fisher*, 1953] (Table 2). All site mean directions are well defined with $k \geq 90$ and $\alpha_{95} \leq 8.1°$. Typical orthogonal projections and stereoplots with the resulting sample directions as well as the mean directions of each locality are given in Figure 6.

[20] Both sites at El Pasajiron as well as sites MBL1, MBD1 and MBU1 show northerly declinations D with somewhat varying inclinations I between 35.3° and 50.1°. This shows that not only the sites at El Pasajiron as well as MBD1 and MBU1 were cooled *in situ*, but also that the block at MBL1 did not rotate after cooling below T_C. At MBL1 two outliers (MBL1-5B and MBL1-6C) show eastward directions. Rock magnetically there is no obvious difference with the other samples. However, already in the field we have noted that reorientation of these samples may be difficult. Thus, these directions were not used for calculation of mean values. Further, data from site MBT1 was not included in the calculations as samples show varying directions throughout the section. Paleodirectional data of this site and a more detailed analysis can be found in Table 3 and section 7.1. Taken together EPJ1 and EPJ2 give a mean direction for the 750 ka El Pasjiron with a declination of 359.7° and an inclination of 39.1°, while MBL1, MBD1 and MBU1 yield D = 357.4° and I = 47.7° for the 2 ka Montaña Blanca.

6. Paleointensity Determination

[21] In the following we concentrate on results for MB, while in section 7.2 data from EPJ are presented.

6.1. Thellier-Type Experiments

[22] Paleointensity experiments on 5 mm and 8 mm diameter miniature cores were done in a MMTD20 thermal demagnetizer. For in-field steps laboratory fields of 30 ± 0.1 μT were applied during heating and cooling. The experiments followed the modified Thellier-technique MT4 [*Leonhardt et al.*, 2004a] for which zero-field steps are done first and which incorporates the commonly used pTRM checks, additivity checks [*Krása et al.*, 2003] and pTRM

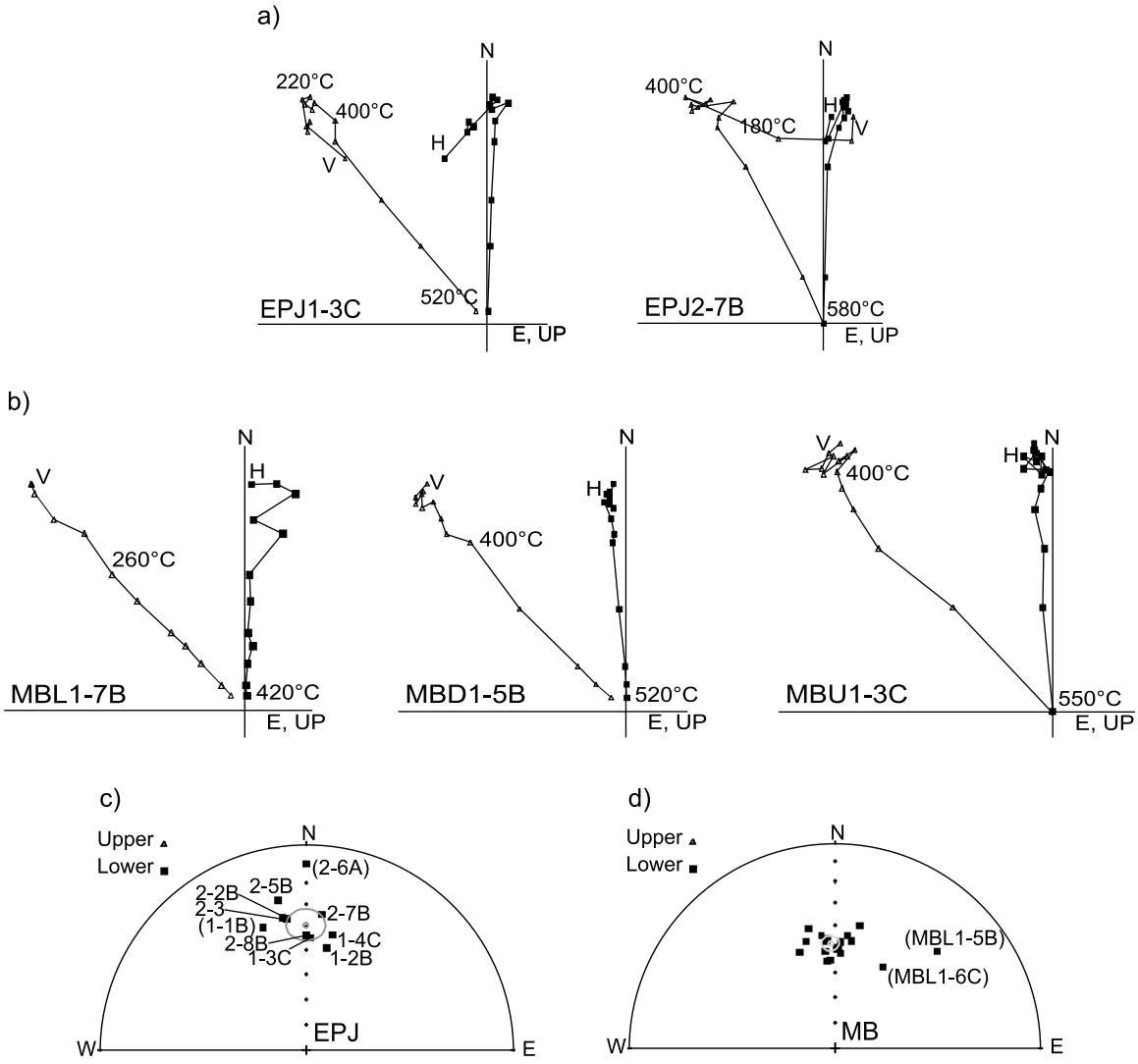

Figure 6. Orthogonal projections of one specimen per site at (a) El Pasajiron (EPJ) and (b) Montaña Blanca (MB). V and H indicate vertical and horizontal components, respectively. (c and d) The stereographic projections of the different specimen directions and the calculated means (grey) of EPJ and MB. Specimen names in brackets mark directions not used for calculation of mean.

tail checks [*Riisager and Riisager*, 2001]. Directional differences between the applied field and the NRM of the pTRM-tail check are taken into account according to *Leonhardt et al.* [2004b]. All determinations were analyzed using the ThellierTool4.21 software and its default criteria [*Leonhardt et al.*, 2004a]. This software allows full-vector treatment and application of check correction. Paleointensity data are summarized in Table 4, additionally quality parameters can be found in Tables S2 and S3 of the auxiliary material, and respective plots of each site are given in Figure 7.

[23] Paleointensity determinations at sites MBU1, MBL1 and MBD1 are of good quality, giving a high success rate of 81% with 17 successful determinations out of 21 that had been performed. Four of these are class A and ten class B results according to the default criteria by *Leonhardt et al.* [2004a]. Further three class C results were used due to good in-site agreement. For most of these determinations fractions f of the NRM [*Coe et al.*, 1978] ≥0.82, only in two cases $f = 0.67$ (MBL1-1C) and $f = 0.41$ (MBD1-2D), were analyzed. Only for sample MBD1-2D has the whole range of the characteristic remanence seen in orthogonal projections not been analyzed. Gap factors g [*Coe et al.*, 1978] are greater than 0.6, in most cases greater even than 0.7, and quality factors q [*Coe et al.*, 1978] range between 7.5 and 141.5, mostly greater than 25. pTRM tails show no multi-

Table 3. Paleodirections of MBT1[a]

Specimen From MBT1	D (deg)	I (deg)
MBT1-2C	298.3	−1.8
MBT1-4B	325.4	−3.5
MBT1-7C	357.5	50.4
MBT1-8B	352.1	61.8
MBT1-10C	14.2	70.3
MBT1-12C	144.3	67.0
MBT1-14B	298.7	36.9

[a]D and I as determined for specimens from MBT1.

Table 4. Paleointensity Results and Correction[a]

Sample	Uncorrected Paleointensity: H_{UC} (μT)	ATRM Correction		CR Correction	
		f_{ATRM}	H_{ATRM} (μT)	f_{CR}	$H_{ATRM,CR}$ (μT)
MBL1-1C	70.2 ± 4.7				
MBL1-2C	61.0 ± 1.7	1.154 ± 0.019	70.4 ± 3.2	-	
MBL1-3C	71,9 ± 1.3	0.955 ± 0.055	68.6 ± 5.1	-	
MBL1-4C	63,9 ± 1.8	1.026 ± 0.005	65.6 ± 2.2	-	
MBL1-5C					
MBL1-6A					
MBL1-7D	71.0 ± 0.7	0.941 ± 0.027	66.8 ± 2.6	-	
MBL site mean	**67.6 ± 4.8**		**67.8 ± 2.1**		
MBD1-1A	65.2 ± 1.2	0.979 ± 0.001	63.8 ± 1.2	-	
MBD1-1AD	72.8 ± 0.8	0.995 ± 0.037	72.4 ± 3.5	-	
MBD1-2D	73.8 ± 1.3	0.934 ± 0.013	68.9 ± 2.2	1.215 ± 0.076	56.7 ± 1.8
MBD1-3C	61.7 ± 1.2				
MBD1-4D	63.2 ± 2.0				
MBD1-5C	64.0 ± 0.3	1.014 ± 0.001	64.9 ± 0.3	1.715 ± 0.070	37.8 ± 1.4
MBD1-6D	52.4 ± 0.7	1.360 ± 0.036	71.3 ± 2.8	1.596 ± 0.035	44.7 ± 0.8
MBD1-7D					
MBD1-8C					
MBD site mean	**64.7 ± 7.2**		**68.3 ± 3.8**		**46.4 ± 9.6**
MBT1-1C					
MBT1-3C	*62.2 ± 0.9*	*1.098 ± 0.060*	*68.3 ± 4.7*	*1.466 ± 0.104*	*46.6 ± 0.1*
MBT1-4C					
MBT1-5A	*65.7 ± 1.1*	*1.225 ± 0.053*	*80.5 ± 4.9*	*1.406 ± 0.033*	*57.2 ± 2.1*
MBT1-6D	69.5 ± 1.8	0.991 ± 0.002	68.9 ± 1.9	1.373 ± 0.092	50.2 ± 2.0
MBT1-8C	*62.5 ± 1.3*	*0.997 ± 0.003*	*62.3 ± 1.5*	*1.484 ± 0.074*	*42.0 ± 1.1*
MBT1-9	80.2 ± 3.7	0.951 ± 0.021	76.3 ± 5.2	1.282 ± 0.035	59.5 ± 2.4
MBT1-10E	70.8 ± 1.9	0.975 ± 0.007	69.1 ± 2.3	1.263 ± 0.029	54.7 ± 0.5
MBT1-11A	*56.1 ± 0.9*	*0.986 ± 0.003*	*55.3 ± 1.0*	*1.188 ± 0.023*	*46.6 ± 0.0*
MBT1-12D	*63.7 ± 3.0*	*1.033 ± 0.000*	*65.8 ± 3.1*	*1.162 ± 0.050*	*56.6 ± 0.2*
MBT1-13A	67.9 ± 0.6	0.973 ± 0.008	66.1 ± 1.1	1.150 ± 0.027	57.4 ± 0.4
MBT1-14C	64.3 ± 0.8	0.993 ± 0.000	63.8 ± 0.8	1.146 ± 0.016	55.7 ± 0.0
MBT site mean	**70.5 ± 5.9**		**68.8 ± 4.7**		**55.5 ± 3.5**
MBT site mean (rot.)	***66.3 ± 6.5***		***67.7 ± 7.0***		***52.7 ± 5.9***
MBU1-1D	65.6 ± 1.3	0.994 ± 0.003	65.2 ± 1.5	1.298 ± 0.072	50.2 ± 1.6
MBU1-2D	62.9 ± 2.5	0.955 ± 0.001	60.1 ± 2.4	-	
MBU1-3C	67.0 ± 1.4	1.038 ± 0.006	69.6 ± 1.9	1.427 ± 0.030	48.8 ± 0.3
MBU1-4D	60.2 ± 3.7	1.087 ± 0.054	65.4 ± 7.3	1.569 ± 0.110	41.7 ± 1.8
MBU1-5C	61.0 ± 1.5	0.953 ± 0.007	58.2 ± 1.9	1.298 ± 0.074	44.8 ± 1.1
MBU site mean	**63.3 ± 2.9**		**63.7 ± 4.6**		**46.4 ± 3.9**
MB loc. mean (without MBT1)	**64.9 ± 1.3**		**67.0 ± 1.3**		**46.4 ± 0.0**
MB loc.mean (with unrot. MBT1)	**66.0 ± 1.6**		**67.3 ± 1.0**		**50.4 ± 3.2**
MB loc. mean (including MBT1)	***65.1 ± 1.0***		***67.1 ± 1.0***		***48.4 ± 2.1***

[a]H_{UC}, H_{ATRM} and $H_{ATRM,CR}$ are the paleointensity values of the individual samples with associated errors for the uncorrected, ATRM corrected and ATRM and cooling rate (CR) corrected determinations, respectively. H_{ATRM} errors are calculated as maximum-minimum errors including the uncertainty of the uncorrected paleointensity σ_{UC} and of the ATRM correction factor f_{ATRM}. $H_{ATRM,CR}$ errors are calculated via full error propagation using the uncertainties of H_{UC}, f_{ATRM} and f_{CR}. Also shown are arithmetic means and standard deviations of the different sites and weighted means for the whole Montaña Blanca locality (in bold, using 1/(arithmetic standard deviation of site means) as weighting parameter; indicated as loc. mean). Data from rotated samples at site MBT1 is shown in italics and for site means indicated by (rot.). For locality MB paleointensity values are given that first are without MBT1, then are including unrotated MBT1 samples and then are including all MBT1 samples.

domain (MD; both tail parameter $\delta(t)$ and relative intensity difference between repeated thermal demagnetizations $\delta(TR) > 7\%$) and only in two cases (MBU1-2D, MBU1-4D) minor PSD ($2\% < (\delta(t)$ and $\delta(TR)) < 7\%$) contribution. Alteration is seemingly absent in most specimens, as difference ratios DRAT [*Selkin and Tauxe*, 2000] are less than 4.3%.

[24] Arithmetic means and standard deviations calculated from the paleointensity results of the different specimens yield mean values of 67.6 ± 4.8 μT for MBL1, 64.7 ± 7.2 μT for MBD1 and 63.3 ± 2.9 μT for MBU1, which within error are identical. The weighted mean paleointensity (weighting factor: 1/standard deviation of the different sites) for Montaña Blanca using the data of these three sites gives 64.9 ± 1.3 μT.

6.2. Magnetic Anisotropy

[25] A rock may be magnetically anisotropic, i.e. its ability to acquire a magnetization in a magnetic field can depend on the direction of this field. High B_{cr} values as determined during rock magnetic experiments suggest shape anisotropy in our samples. Fortunately, as weak field TRM is proportional to the field strength, the anisotropy tensor of TRM (ATRM tensor) can be obtained.

[26] Such determinations of the ATRM tensor were done on the same samples as previous paleointensity determinations, using again the MMTD20 demagnetizer. TRMs were imparted using in-field heating/cooling cycles to the upper end of the blocking spectra of the samples subsequently in +z, +x, −x, +y, −y and −z direction. Additionally, the +z treatment was repeated in the end to check for alteration. The

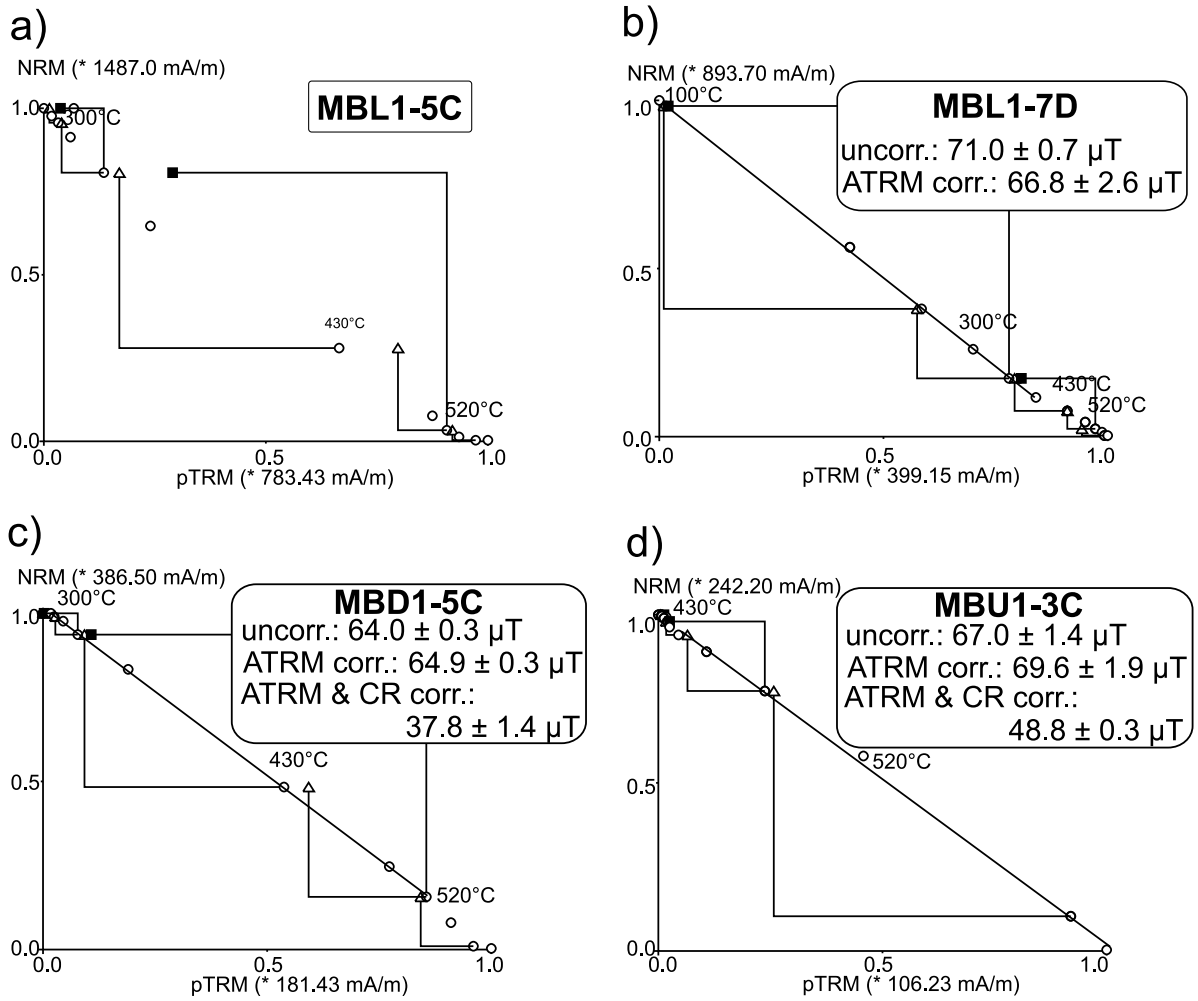

Figure 7. Respective NRM/pTRM diagrams (triangles: alteration checks, squares: additivity checks) for sites MBL1 (MBL1-5C rejected, MBL1-7D accepted), MBD1 and MBU1. Uncorrected and whenever possible ATRM and ATRM plus cooling rate (CR) corrected paleointensity values of the specimens are given.

measurements were analyzed following the approach of *Veitch et al.* [1984] and the results are again summarized in Table 4. After determining the ATRM tensor, the direction of the ancient field was calculated and the scaling factor f_{ATRM} to adjust the measured paleointensity by $H_{ATRM} = H_{UC} * f_{ATRM}$ (UC: uncorrected), is finally obtained by the relationship between ancient magnetization acquisition and laboratory magnetization acquisition in dependence of the ATRM tensor. An error estimate was obtained by not only determining f_{ATRM} from the averaged axes components but also separately for positive (+x, +y, +z) and negative (−x, −y, −z) measurements, i.e. f^{pos}_{ATRM} and f^{neg}_{ATRM}. This way orientation errors and slight mineralogical changes are accounted for. The uncertainty of f_{ATRM} is then calculated by $\sigma(f_{ATRM}) = (|f^{pos}_{ATRM} - f^{neg}_{ATRM}|)$. The uncertainty σ_{ATRM} of the ATRM corrected intensity H_{ATRM} is a minimum/maximum error including the uncertainty of the paleointensity determination and of f_{ATRM}.

[27] Relative differences in +z measurements are smaller than 3% and anisotropy correction could be performed (Table 4). For samples MBL1-1C, MBD1-3C and MBD1-4D no anisotropy or cooling (section 6.3) experiments were done. The resultant scaling factors f_{ATRM} of the other samples range between 0.93 and 1.36, although the majority of scaling factors is close to 1. For sites MBL1 and MBU1 resulting ATRM corrected mean paleointensities (again arithmetic mean and standard deviation) are almost the same as before correction: 67.8 ± 2.1 μT (0.2% higher) and 63.7 ± 4.6 μT (0.6% higher) respectively. However, at site MBD1 a 5.6% higher corrected value of 68.3 ± 3.8 μT is observed. Within site scatter at MBL1 and MBD1 is reduced by anisotropy correction while at MBU1 a higher error after correction is observed. Taking all three sites together a slightly larger (3.2%) weighted mean paleointensity of 67.0 ± 1.3 μT is observed for Montaña Blanca after correction compared to the uncorrected value of 64.9 ± 1.3 μT. Within error both values are identical and the error stays the same. This is due to the only marginal influence of ATRM scaling.

6.3. Cooling Rate Dependence

[28] All our data suggest that we are dealing with remanence carriers within or close to the SD range. Theoretically [*Halgedahl et al.*, 1980; *Dodson and McClelland-*

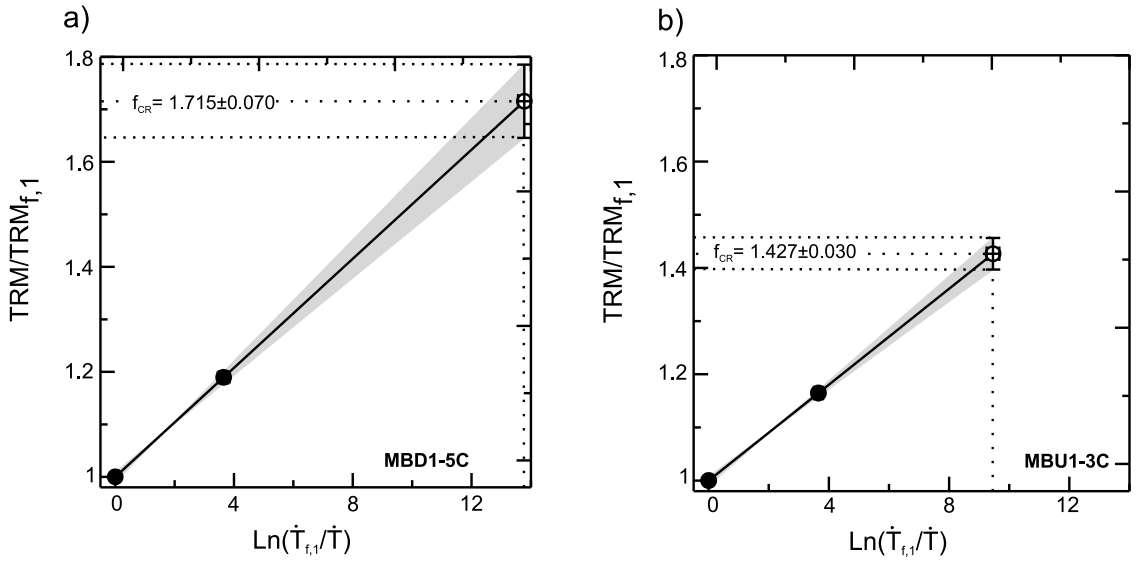

Figure 8. Cooling rate correction using the laboratory measured cooling rate dependency (solid symbols) and related uncertainties, as well as the linear extrapolation of the TRM dependency to the natural cooling rates as determined by relaxation geospeedometry (open symbols) for samples MBD1-5C and MBU1-3C.

Brown, 1980] and experimentally [*Fox and Aitken*, 1980; *McClelland-Brown*, 1984] it was found that an assemblage of identical, non-interacting SD particles acquires a larger TRM during slower cooling. However, even when dealing with only SD particles, the cooling rate dependency of TRM acquisition is not constant, but depends already on small changes in grain size and domain state. *Leonhardt et al.* [2006] and *Ferk et al.* [2010] showed that experiments which give the TRM dependency on cooling rate together with determinations of natural cooling rates from relaxation geospeedometry have to be done to correct overestimation of paleointensity.

[29] Following the approach by *Leonhardt et al.* [2006], the same specimens as for Thellier-Thellier and anisotropy experiments were subjected to magnetic cooling rate dependency investigations that included two laboratory cooling rates. For fast cooling the cooling fan of the MMTD20 furnace was used like during the previous experiments, while for slow cooling the samples were cooled without fan operation. Laboratory cooling rates were determined on basaltic dummy samples across the glass transition intervals of our samples, i.e. between about 700°C and 550°C. By monitoring the temperature decrease versus time (using a thermocouple inside one of the basaltic samples) the mean cooling rates of our furnace in this temperature range were determined, i.e. the slope of the temperature decrease versus time curve between 700°C and 550°C was determined. A conservative estimate of the uncertainty in cooling rate determination is 10% for fast cooling and 5% for slow cooling.

[30] First, a fast heating/cooling cycle with a cooling rate of ~385 K/min was used to impart a TRM (TRM$_{f,1}$). Then a heating/cooling cycle with a 38.5-fold slower cooling rate of ~10 K/min (TRM$_{s,1}$) and at the end, another fast one (TRM$_{f,2}$) in order to check for alterations during the experiment, were done. TRM$_{f,1}$ and TRM$_{f,2}$ of most samples differ by ≤2% indicating no or very small alterations. Only four samples show differences of up to 5%. However, these samples also show differences between TRM$_{f,1}$ and TRM$_{s,1}$ ≥20% and thus, alteration in these samples should still be small enough to enable cooling rate corrections. Differences between TRM$_{f,1}$ and TRM$_{f,2}$ are used as error estimates for TRM$_{s,1}$ and TRM$_{f,1}$.

[31] The TRM intensity for slow cooling is 7% to 31% larger than for fast cooling. This is higher than the theoretically predicted 5% to 7% overestimate per order of magnitude [*Halgedahl et al.*, 1980; *Dodson and McClelland-Brown*, 1980]. TRM overestimates exceeding the theoretically predicted values were also observed for example in a study by *Genevey and Gallet* [2002] on archeomagnetic materials. A possible reason for the here observed overestimates of up to 31%, could be related to low-titanium titanomagnetites as remanence carriers and not SD magnetite or hematite as used in the theoretical studies. Titanomagnetites are characterized by different magnetic parameters, of which in particular the blocking temperature relationship, relaxation times and anisotropy are relevant for cooling rate dependencies.

[32] The magnetic cooling rate dependency is extra-/interpolated to the natural cooling rates as determined by relaxation geospeedometery to correct the overestimation of the H_{ATRM} values (interpolation only for MBT1-14C which has a natural cooling rate of 12 K/min). To do this, the laboratory measured TRM$_{f,1}$ and TRM$_{s,1}$, both normalized to TRM$_{f,1}$, are plotted versus ln($\dot{T}_{f,1}/\dot{T}$) (Figure 8). According to *Halgedahl et al.* [1980] such linear extra-/interpolation is valid, if the remanence carriers are non-interacting SD particles that dominantly block close to the respective blocking temperature. As our samples are at least close to SD and unblock sharply within about 100 to 150°C, these conditions are fulfilled. The previous error estimates for inaccuracy of laboratory cooling rate and magnetization determinations allow a minimum/maximum error propagation towards the natural cooling rates (Figure 8). The obtained cooling rate

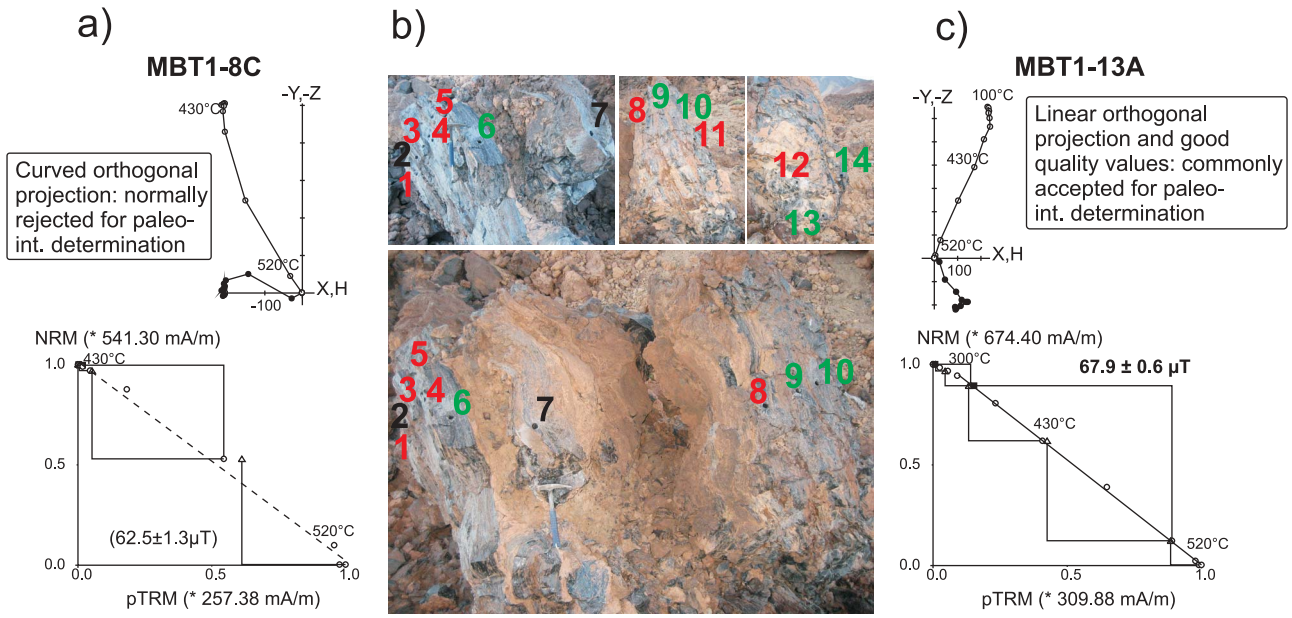

Figure 9. NRM/pTRM diagrams and respective orthogonal projections from the profile at MBT1. (a) Plots of sample MBT1-8C, which normally would be rejected for paleointensity determination due to curved orthogonal projection. (b) Pictures of MBT1 showing samples that are commonly accepted (green) and rejected (red) for paleointensity determination. (c) Plots of sample MBT1-13A, which was accepted for paleointensity determination as orthogonal projection is linear and quality parameters were good.

correction factor f_{CR} = TRM/TRM$_{f,1}$ is then used to correct the paleointensity values H_{ATRM} by

$$H_{ATRM,CR} = \frac{H_{ATRM}}{f_{CR}}. \quad (1)$$

[33] Full error propagation, including the uncertainties of the paleointensity experiments as well as those of f_{ATRM} and f_{CR} gives the uncertainty $\sigma_{ATRM,CR}$ of the individual ATRM and cooling rate corrected paleointensity values. An application of cooling rate correction was only possible for samples whose natural cooling rates were determined successfully by relaxation geospeedometry. Thus, no cooling rate correction was possible for site MBL1 where the high crystal content suppressed any peak during calorimetry. At the other sites H_{ATRM} values are significantly reduced (Table 4). This results in arithmetic mean values of 46.4 ± 9.6 μT at MBD1, 46.4 ± 3.9 μT at MBU1 and a weighted mean value (weighting factor: 1/standard deviation of the different sites) of 46.4 ± 0.0 μT for whole Montaña Blanca. The ~20 μT reduction (28.5% for whole Montaña Blanca) relative to the non-corrected values underlines the pivotal importance of cooling rate correction for SD dominated materials.

7. Discussion

7.1. Emplacement Rotations at Site MBT

[34] Some specimens of MBT1 show acquisition of TRM during emplacement rotations/squeezing and block break-ups while cooling. This can be seen clearly in the curved orthogonal projections of the Thellier measurements (Figure 9a) and is verified by field observation (Figure 9b) and associated paleomagnetic directions (Table 3): Specimens MBT1-7C, MBT1-8B and MBT1-10C from the inner parts, which were the last to cool below T_C give northerly directions with inclinations between 50° and 70° (expected inclination for a GAD, i.e. for a geoaxial dipole: 46.8°). This corresponds relatively well to D = 357.4° and I = 47.7° for the other sites at MB. Thus, the inner part seems to be almost in the same position as during cooling. However, this does not account for the outer parts, where directions far from normal are recorded. At the left end of the site D = 298.3°, I = −1.8° (MBT1-2C) and D = 325.4°, I = −3.5° (MBT1-4B) are observed, while at the right end D = 144.3°, I = 67.0° (MBT1-12C) as well as D = 298.7°, I = 36.9° (MBT1-14B) are found.

[35] Such rotations will not affect the resultant paleointensity if cooling occurs during a "normal" time range, i.e. external field variations are negligible. However, Arai plots with associated curved orthogonal projections are normally disregarded for paleointensity determination. Therefore, at first, only the paleointensity of specimens with linear parts in the orthogonal projections were analyzed (e.g., Figure 9c), yielding a uncorrected mean value for MBT1 of 70.5 ± 5.9 μT, an anisotropy corrected value of 68.8 ± 4.7 μT and a ATRM and CR corrected value of 55.5 ± 3.5 μT.

[36] Arai plots of specimens with curved orthogonal projections, however, are often of very similar quality as those of the other MBT1 samples. Both samples with curved and with linear orthogonal projections show fraction of the NRM f ≥ 0.84, only two times it is as low as 0.7 (MBT1-9) and 0.66 (MBT1-10E). MBT1-9 also shows a relatively low gap factor g = 0.44 while all the other samples have g ≥ 0.64. The quality factor q is mostly >16, again only MBT1-9 shows a low q = 6.7 value. Taken together these data correspond to two class A, seven class B and only one class C

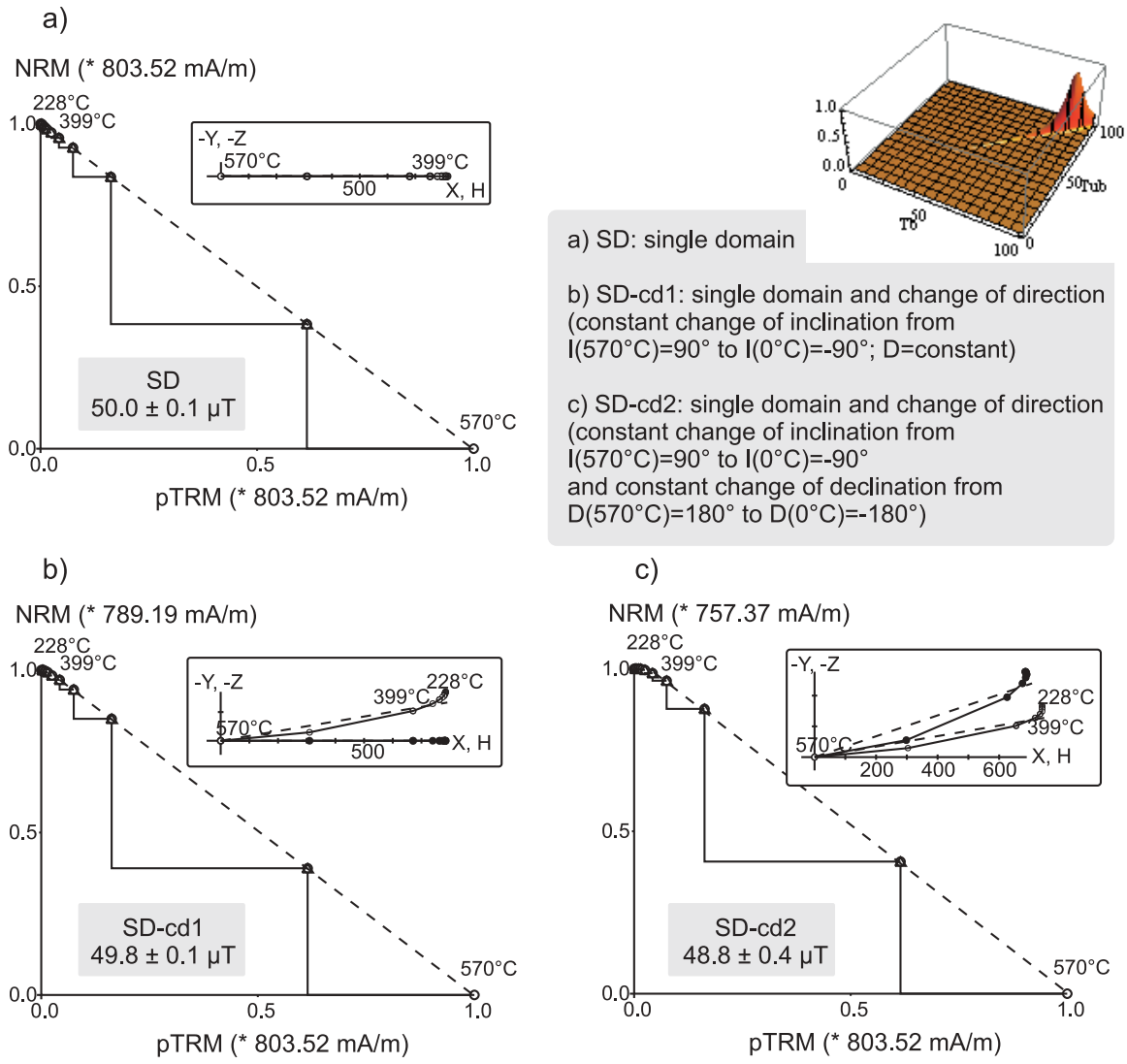

Figure 10. NRM/pTRM diagrams as calculated for a sample with SD remanence carriers (with minor MD contribution, shown in the inset), that (a) was not rotated during emplacement, (b) shows an constant change in inclination, and (c) shows constant changes in inclination and declination. Figures 10a and 10b yield true paleointensity of 50 μT, while Figure 10c gives slightly too low value.

result according to *Leonhardt et al.* [2004a]. Due to the good quality of Arai plots of rotated samples, it was checked whether these data can be used by applying some pTRM model calculations using the phenomenological model by *Leonhardt et al.* [2004b] including some modification according to *Fabian and Leonhardt* [2010] (Figure 10). If no rotations are implied the model yields the true "paleo" intensity (50 μT) for a SD remanence carrier (Figure 10a). When only inclination changes constantly from 90° at 570°C to −90° at 0°C, while declination is kept constant, a slightly lower but within error true value is calculated (Figure 10b). A constant change in direction during the whole cooling was applied as this is easily done in the computer calculation and gives a similar directional change during the blocking process as is observed in our samples. If, additionally, declination changes constantly from 180° at 570°C to −180° at 0°C the intensity is underestimated by 1.2 μT (Figure 10c). However, this results from the fact that a slight MD contribution has to be introduced to the model (inset in Figure 10) to enable computer calculations. Taken together, for SD remanence carriers paleointensity data from specimens with curved orthogonal projections should be reliable. Thus, taking these data into account a mean value of 66.3 ± 6.5 μT is obtained.

[37] However, if the recording material is anisotropic, as it is the case for many of our samples, then those coeval cooling rotations may become a nuisance. Usually, as mentioned before (section 6.2) anisotropy corrections are conducted using the ATRM tensor and the average direction of the selected linear segment in the Arai diagram, i.e. the resultant paleointensity is corrected. This technique may not be applicable when continuous changes of TRM acquisition directions are occurring. Indeed, it should be necessary to apply the anisotropy correction at each individual thermal step and its associated direction. This was done for all rotated MBT1 samples. As can be seen in Figure 11 the

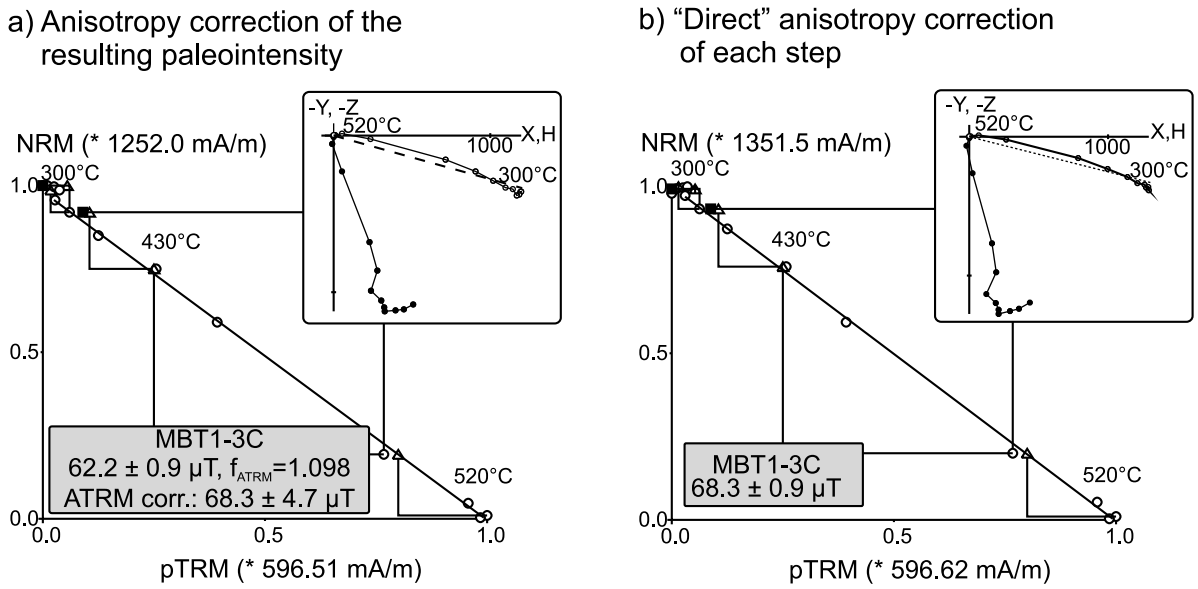

Figure 11. NRM/pTRM diagrams for MBT1-3C with anisotropy correction of (a) the resultant paleointensity and (b) each thermal step and the respective directions.

paleointensity values do not change when comparing anisotropy correction of each step with anisotropy correction of the resultant paleointensity. Only uncertainty ranges are different, as for the latter (Figure 11a) errors of both the paleointensity determination and of the correction factor are included, while for the former (Figure 11b) only the one of the paleointensity determination is included and the errors of the different correction factors for each step are left out. At least for samples with relatively small anisotropies a correction of the resultant paleointensity is therefore reasonable, which gives an anisotropy corrected mean value for MBT1 of 67.7 $\pm$ 7.0 μT when all samples are included. Additional application of CR correction gives an paleointensity of 52.7 $\pm$ 5.9 μT. As all the data from site MBT1 are quite reasonable, they can also be included in calculation of an ATRM and CR corrected mean value for MB (including all samples from MBT1) yielding a ancient field value of 48.4 $\pm$ 2.1 μT.

7.2. Devitrification at El Pasajiron

[38] It was not possible to get good quality paleointensity data for El Pasajiron. Respective data (paleointensity values and quality parameters) can be found in Table S3 in the auxiliary material. Alteration occurs during all paleointensity experiments on samples from EPJ1. Nevertheless, if one analyzes the measurements, high paleointensity values of 60 to 68 μT are obtained. At EPJ2 alteration is not as strong as at EPJ1. However, increasing values of 17 to 38 μT are found for EPJ2-2B to EPJ2-6B (Figure 12e) with especially the Arai plot of EPJ2-4C (28.7 $\pm$ 0.6 μT) being of (seemingly) very high quality (Figure 13a). EPJ2-7C and EPJ2-8C behave very similar to samples from EPJ1. They also yield high field values ($\sim$71 μT and $\sim$65 μT, respectively) and show non-linearity and failing pTRM checks which we interpret as alteration (Figure 13b). No paleointensity value could be obtained for EPJ2-1C. To understand this at first

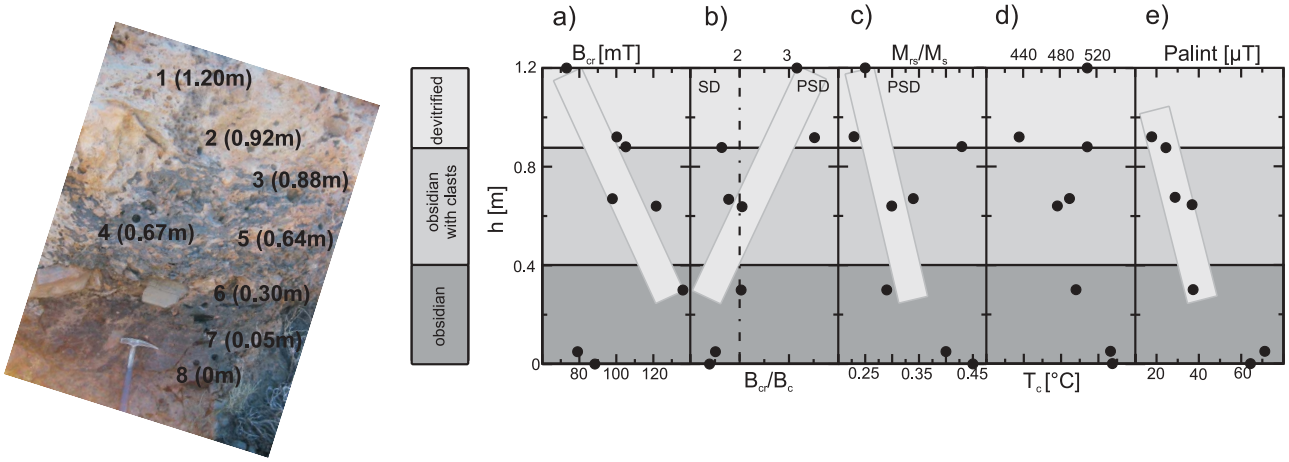

Figure 12. (a–e) Picture of site EPJ2 together with rock magnetic parameters and paleointensity values across the profile. Diagonal boxes in Figures 12a–12c and 12e show trends in data.

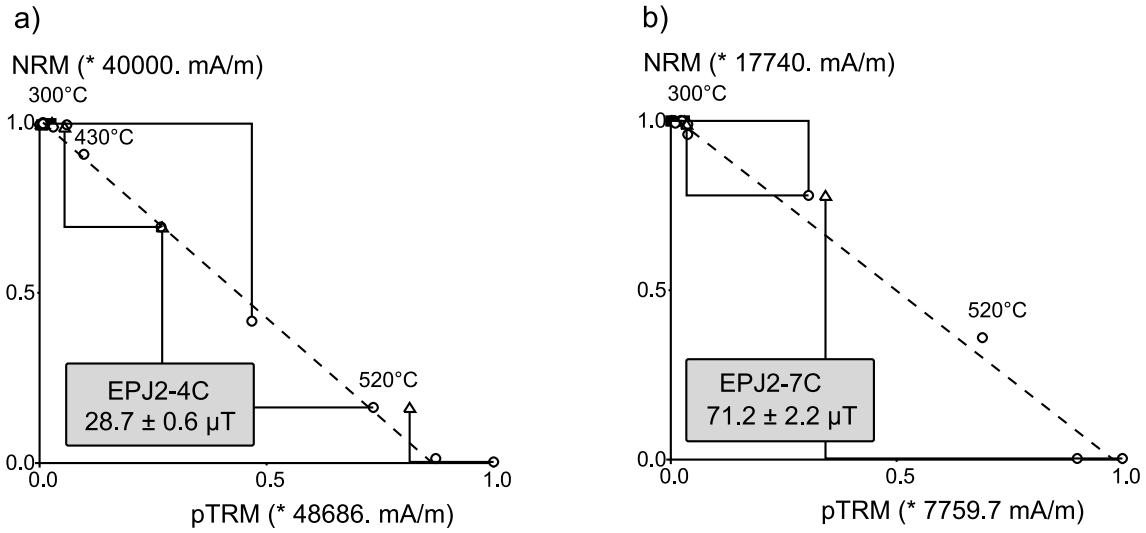

Figure 13. No obvious difference in quality can be found between paleointensity determinations of samples that (a) show CRM overprint or (b) carry the original TRM.

sight astonishing variation in data, a closer look at the profile EPJ2 is needed: Site EPJ2 changes from clearly devitrified at the top to more glassy samples at the bottom. Both a picture of site EPJ2 and different rock magnetic parameters and values for paleointensity vs. profile height can be found in Figure 12. It is important to mention that even though the profile changes from devitrified to more glassy, this may not account for each sample as during sampling we tried to find glassy parts even in the upper third. Further, there are differences between the surface and the inside of the rock. Some changes in rock magnetic parameters with increasing alteration are observed. B_{cr} appears to get smaller with the increasing hydration from samples EPJ2-6B to EPJ2-1C (Figure 12a). However, samples EPJ2-7C and EPJ2-8A show B_{cr} values almost as low as EPJ2-1C. Further, there is a trend towards more PSD-like behavior with increasing hydration (Figures 12b, 12c, and 5d). EPJ2-1C and EPJ2-2D are in the PSD range of the Day plot, while EPJ2-7C, EPJ2-8A and interestingly also EPJ2-3 have almost the same close to SD hysteresis parameters as samples from EPJ1. EPJ2-4C to EPJ2-6B already show a trend towards the two samples in the PSD range. There is no change in T_C that can be directly correlated to the change in devitrification (Figure 12d).

[39] Taken together, the rock magnetic and paleointensity data suggest that during devitrification of the upper part of EPJ2 either new remanence carriers have grown or the old ones were altered, both leading to a change in NRM due to acquisition of a chemical remanence (CRM). Especially the increasing paleointensity values from the most devitrified samples to the more glassy samples support this hypothesis. The identical directions of EPJ1 and EPJ2 do not contradict this suggestion as northerly directions are found for the whole Brunhes chron and a later acquired CRM would give approximately the same direction as the primary remanence. Devitrified samples like EPJ2-4C carry a CRM which cannot be seen in the Arai plot and gives wrong paleointensities. The true field value at Tenerife 750 ka ago can only be obtained by those samples that are not devitrified. Hence, the field strength seems to have been approximately 60 to 70 μT (without inclusion of cooling rate dependency). However, as alteration is present in all samples yielding these high field values, calculation of a mean paleointensity for this time is not justified and further investigations, e.g. at other not devitrified sites at the Caldera Wall, are needed to get a reliable paleointensity value.

[40] Even though paleointensity experiments for EPJ failed, it was tried to determine the ATRM tensor for samples from EPJ1 and EPJ2 to check whether the high differences in paleointensity are partly connected to anisotropy within the samples. However, a 2% to 10% difference in the two +z measurements indicates alteration and a meaningful determination of the ATRM tensor and of f_{ATRM} is, thus, not possible. As both paleointensity and anisotropy experiments for El Pasajiron sites had failed, no cooling rate experiments were done on these samples.

7.3. Comparison of MB Data With Those of Other Studies

[41] Inclusion of the data from the rotated site MBT1 gives an ATRM and cooling rate corrected paleointensity value of 48.4 ± 2.1 μT. This corresponds to a Virtual Dipole Moment (VDM) of 9.64 ± 0.42 *10^{22}Am^2 (uncertainty is a minimum/maximum error using the error bonds of the paleointensity, Table 5). Further, declination D = 357.4° and inclination I = 47.7° corresponding to a Virtual Geomagnetic Pole (VGP) of 87.7°N and 266.8°E were obtained. These values compare very well to both geomagnetic models and older paleointensity data (Table 5): The geographically closest paleomagnetic data for this time are some brick samples from Spain (54 ± 24 BCE) [*Kovacheva et al.*, 1995] that yield a paleointensity of 60.9 ± 1.7 μT which corresponds to a VDM of 10.63 ± 0.58 *10^{22}Am^2 and baked clay (200 ± 100 BCE) and brick (50 ± 50 BCE) from Morocco [*Kovacheva*, 1984, 1985] with paleointensities of 56.6 ± 5.3 μT and 61.2 ± 1.3 μT and VDMs of 10.57 ± 1.64 * 10^{22}Am^2 and 11.25 ± 0.69 *10^{22}Am^2, respectively. No cooling rate or anisotropy correction were made for any of these data, though *Kovacheva et al.* [1995] explain that for

Table 5. VGPs, VDMs, and VADMs of Archeomagnetic Studies and Geomagnetic Models at ~115 BCE[a]

Data Set	Age (AD)	Location	D (deg)	I (deg)	Int. (μT)	VGP Latitude (°N)	VGP Longitude (°E)	VDM (10^{22}Am^2)	VADM (10^{22}Am^2)
This study	−115 ± 17	Tenerife	357.4	47.7	48.4 ± 2.1	87.7	266.8	9.64 ± 0.42	9.71 ± 0.42
Kovacheva et al. [1985]	−54 ± 24	Spain	359.2	58.4	60.9 ± 1.7	86.8	189.1	10.63 ± 0.58	10.26 ± 0.29
Kovacheva [1984, 1985]	−200 ± 100	Morocco	1.8	53.0	56.6 ± 5.3	87.6	136.0	10.57 ± 1.64	10.32 ± 0.97
Kovacheva [1984, 1985]	−50 ± 50	Morocco	353.9	54.3	61.2 ± 1.3	85.0	258.1	11.25 ± 0.69	11.16 ± 0.24
Bayesian inversion model	−100	Tenerife	1.7	43.1	47.3 ± 3.2	86.5	138.1	9.89 ± 0.67	9.48 ± 0.64
Bayesian inversion model	−120	Tenerife	2.1	42.7	47.7 ± 3.4	86.0	134.6	10.0 ± 0.71	9.57 ± 0.68
ARCH3K.1	−120	Tenerife	2.6	46.3	49.5	87.6	87.6	10.0	9.93
ARCH3K.1	−110	Tenerife	2.0	46.0	49.6	88.0	98.9	10.1	9.95
CALS3K.3	−120	Tenerife	1.2	44.4	51.3	87.6	137.5	10.6	10.29
CALS3K.3	−110	Tenerife	1.3	44.3	51.1	87.5	136.1	10.6	10.25
CALS7K.2	−120	Tenerife	357.9	43.6	46.4	86.6	197.8	9.67	9.32
CALS7K.2	−110	Tenerife	357.9	43.3	46.2	86.5	195.8	9.65	9.28

[a]Locations, together with declination D, inclination I, paleointensity Int., virtual geomagnetic poles (VGP latitude and longitude), virtual dipole moments VDM and virtual axial dipole moments VADM of this study, 3 archeomagnetic studies (Spain: 42.27°N, 357.98°E [*Kovacheva et al.*, 1995; *Parés et al.*, 1992], Morocco: 35.50°N, 354.00°E [*Kovacheva*, 1984, 1985]) and four geomagnetic models (Bayesian inversion model for last 3000 years [*Leonhardt et al.*, 2010], ARCH3K.1 [*Donadini et al.*, 2009], CALS3K.3 [*Korte et al.*, 2009] and CALS7K.2 [*Korte and Constable*, 2005]; all computed for Tenerife: 28.25°N, 343.4°E).

the Spanish bricks neither of the two is necessary. As these sites are from more northerly latitudes, the paleointensities are all higher than our data. Two of the VDMs, however, are within error identical to our value and the third one is only slightly higher. This is a very good agreement, especially when the geographical distance and the age difference are taken into account. Additionally, a comparison with different geomagnetic field models by *Leonhardt et al.* [2010], *Donadini et al.* [2009], *Korte and Constable* [2005], and *Korte et al.* [2009] can be done. When these models are run for the geographical longitude and latitude of our sites very good agreement with our data is found, which shows the validity of the geomagnetic models for that time and area. Only paleointensity and VDM data of CAL3K.3 [*Korte et al.*, 2009] are out of the error bounds of our data, though still reasonably close. VGP latitudes of the models are very close to our data as well, whereas VGP longitudes are up to 180° off. This is due to the proximity to geographic north: Even though the poles are very close to each other, strong differences in VGP longitude may be observed. Last but not least, a comparison with today's field intensity at Tenerife, 38.5 μT, shows a decrease in intensity by 20% during the last 2 ka.

8. Conclusion

[42] We have conducted a study of paleodirections and paleointensities on samples from Tenerife. For the 750 ka old El Pasajiron, at the southern Caldera wall, no good data could be obtained as during paleointensity experiments either alteration occurred or potential CRM overprints were found for devitrified samples. When comparing paleomagnetic and rock magnetic data from different samples within the sites the following trends were found with increasing devitrification: Hysteresis and backfield properties showed a trend towards more PSD-like behavior and paleointensity was shown to decrease. A possible explanation for these features is the later acquisition of a CRM. This possible CRM is not easily identified in the paleointensity experiments as it is not monitored by any of the performed checks. Indeed, some of the paleointensity determinations on apparently CRM overprinted samples are of high quality and would normally be regarded as reliable. Due to the possible CRM overprint no trustworthy data can be obtained from the devitrified samples. As the nondevitrified - and, thus, not CRM overprinted - samples altered during paleointensity experiments, their paleointensities can not be used either. However, they all yield values of 60 to 70 μT, hence, suggesting a strong field 750 ka ago. Further investigations for example at other not devitrified sites at the Caldera wall will have to show whether this is true. In conclusion, our data suggest that devitrified samples are prone to CRM overprinting and may not result in reliable paleomagnetic data. However, as our data set is very small and as alteration complicates the situation, further studies will have to prove whether the observed trends are found in other sections and are really connected to devitrification and/or hydration of glass and whether a CRM overprint truly exists. Nonetheless to be on the safe side when working with obsidian one should only sample nondevitrified sites as long as there are no other studies analyzing the reliability of devitrified samples.

[43] Much better results were obtained for samples of the 115 ± 17 BCE Montaña Blanca eruption. Paleointensity experiments are generally of high quality (sections 6.1 and 7.1) and also anisotropy and cooling rate corrections were successful. Emplacement rotations and squeezing structures that are often found at obsidian outcrops were analyzed in detail at site MBT1. It was shown that paleointensity determinations of samples with curved orthogonal projections can be accepted when dealing with SD remanence carriers and that anisotropy correction can still be done for the resulting paleointenstity of our relatively weak anisotropic samples. The data of MBT1 was thus included in an ATRM and cooling rate corrected paleointensity value for whole Montaña Blanca of 48.4 ± 2.1 μT (VDM: 9.64 ± 0.42 *10^{22}Am^2). Taking the geographical distance and age difference into account, the VDM value compares very well to data from Spain (54 ± 24 BCE: 10.63 ± 0.58 * 10^{22}Am^2 [*Kovacheva et al.*, 1995]) and Morocco (200 ± 100 BCE: 10.57 ± 1.64 * 10^{22}Am^2 [*Kovacheva*, 1984], 11.25 ± 0.69 * 10^{22}Am^2 [*Kovacheva*, 1985]). Comparison of the data with geomagnetic field models [*Leonhardt et al.*, 2010; *Donadini et al.*, 2009; *Korte and Constable*, 2005; *Korte*

et al., 2009] shows very good agreement and hence the validity of the models for this time and geographic area is supported.

[44] **Acknowledgments.** We thank Andy Biggin and Lisa Tauxe for their thorough reviews that strongly helped to improve the manuscript. We gratefully acknowledge Joan Marti for sharing his fundamental knowledge about geology and volcanology of Tenerife on the field trip in September 2007. We also thank him for providing the geological map of Tenerife and for giving fast and helpful answers to all our emails. Funding was provided by DFG grant Le1905/1-1 and FWF grant P21221-N14. D. B. Dingwell acknowledges the funding support of a LMU Excellent Research Professorship in experimental Volcanology (Bundesexzellenzinitiative) and ERC advanced grant EVOKES.

References

Ablay, G. J., and J. Marti (2000), Stratigraphy, structure, and volcanic evolution of the Pico Teide-Pico Viejo formation, Tenerife, Canary Islands, *J. Volcanol. Geotherm. Res.*, *103*, 175–208.

Ablay, G. J., G. G. J. Ernst, J. Marti, and R. S. J. Sparks (1995), The 2ka subplinian eruption of Montana Blanca, Tenerife, *Bull. Volcanol.*, *57*, 337–355.

Ancochea, E., J. M. Fuster, E. Ibarrola, A. Cendrero, J. Coello, F. Hernan, J. M. Cantagrel, and C. Jamond (1990), Volcanic evolution of the island of Tenerife (Canary Islands) in the light of new K-Ar data, *J. Volcanol. Geotherm. Res.*, *44*, 231–249.

Bowles, J., J. S. Gee, D. V. Kent, E. Bergmanis, and J. Sinton (2005), Cooling rate effects on paleointensity estimates in submarine basaltic glass and implications for dating young flows, *Geochem. Geophys. Geosyst.*, *6*, Q07002, doi:10.1029/2004GC000900.

Buddington, A. F., and D. H. Lindsley (1964), Iron-titanium oxide minerals and synthetic equivalents, *J. Petrol.*, *5*, 310–357.

Coe, R. S., S. Grommé, and E. A. Mankinen (1978), Geomagnetic paleointensities from radiocarbon-dated lava flows on Hawaii and the question of the Pacific nondipol low, *J. Geophys. Res.*, *83*, 1740–1756.

Day, R., M. D. Fuller, and V. A. Schmidt (1977), Hysteresis properties of titanomagnetites: Grain size and composition dependence, *Phys. Earth Planet. Inter.*, *13*, 260–266.

Debolt, M. A., A. J. Easteal, P. B. Macedo, and C. T. Moynihan (1976), Analysis of structural relaxation in glass using rate heating data, *J. Am. Ceram. Soc.*, *59*(1–2), 16–21.

Dodson, M. H., and E. McClelland-Brown (1980), Magnetic blocking temperatures of single-domain grains during slow cooling, *J. Geophys. Res.*, *85*, 2625–2637.

Donadini, F., M. Korte, and C. G. Constable (2009), Geomagnetic field for 0–3 ka: 1. New data sets for global modeling, *Geochem. Geophys. Geosyst.*, *10*, Q06007, doi:10.1029/2008GC002295.

Dunlop, D. (2002), Theory and application of the Day plot (m_{rs}/m_s versus h_{cr}/h_c): 1. theoretical curves and tests using titanomagnetite data, *J. Geophys. Res.*, *107*(B3), 2056, doi:10.1029/2001JB000486.

Fabian, K., and R. Leonhardt (2010), Multiple-specimen absolute paleointensity determination: An optimal protocol including pTRM normalization, domain-state correction, and alteration test, *Earth Planet. Sci. Lett.*, *297*, 84–94.

Ferk, A., F. W. v. Aulock, R. Leonhardt, K.-U. Hess, and D. B. Dingwell (2010), A cooling rate bias in paleointensity determination from volcanic glass: An experimental demonstration, *J. Geophys. Res.*, *115*, B08102, doi:10.1029/2009JB006964.

Fisher, R. A. (1953), Dispersion on a sphere, *Proc. R. Soc. London, Ser. A*, *217*, 295–305.

Fox, J. M. W., and M. J. Aitken (1980), Cooling-rate dependency of thermoremanent magnetisation, *Nature*, *283*, 462–463.

Geissman, J. W., N. G. Newberry, and D. R. Peacor (1983), Discrete single-domain and pseudo-single-domain titanomagnetite particles in silicic glass of an ash flow tuff, *Can. J. Earth. Sci.*, *20*, 334–338.

Genevey, A., and Y. Gallet (2002), Intensity of the geomagnetic field in western Europe over the past 2000 years: New data from ancient French pottery, *J. Geophys. Res.*, *107*(B11), 2285, doi:10.1029/2001JB000701.

Gottsmann, J., and D. B. Dingwell (2001a), Cooling dynamics of spatter-fed phonolite obsidian flows on Tenerife, Canary Islands, *J. Volcanol. Geotherm. Res.*, *105*, 323–342.

Gottsmann, J., and D. B. Dingwell (2001b), The cooling of frontal flow ramps: A calorimetric study on the Rocche Rosse rhyolite flow, Lipari, Aeolian Islands, Italy, *Terra Nova*, *13*, 157–164.

Gottsmann, J., A. J. L. Harris, and D. B. Dingwell (2004), Thermal history of Hawaiian Pa-hoehoe lava crusts at the glass transition: Implications for flow rheology and emplacement, *Earth Planet. Sci. Lett.*, *228*, 343–353.

Halgedahl, S. L., R. Day, and M. Fuller (1980), The effect of cooling rate on the intensity of weak-field trm in single-domain magnetite, *J. Geophys. Res.*, *85*, 3690–3698.

Henkel, O. (1964), Remanenzverhalten und Wechselwirkung in hartmagnetischen Teilchenkollektiven, *Phys. Stat. Sol.*, *7*, 919–929.

Juárez, M. T., L. Tauxe, J. S. Gee, and T. Pick (1998), The intensity of the Earth's magnetic field over the past 160 million years, *Nature*, *394*, 878–881.

Kirschvink, J. L. (1980), The least-squares line and plane and the analysis of paleomagnetic data, *Geophys. J. R. Astron. Soc.*, *62*, 699–718.

Korte, M., and C. G. Constable (2005), Continuous geomagnetic field models for the past 7 millennia: 2. CALS7K, *Geochem. Geophys. Geosyst.*, *6*, Q02H16, doi:10.1029/2004GC000801.

Korte, M., F. Donadini, and C. G. Constable (2009), Geomagnetic field for 0–3 ka: 2. A new series of time-varying global models, *Geochem. Geophys. Geosyst.*, *10*, Q06007, doi:10.1029/2008GC002295.

Kovacheva, M. (1984), Some archaeomagnetic conclusions from 3 archaeological localities in northwest Africa, *C. R. Acad. Sci. Bulg.*, *37*, 171–174.

Kovacheva, M. (1985), Recherches archéomagnétiques sur trois sites archéologiques du Maroc, *Bull. Archeol. Marocaine*, *19*, 285–293.

Kovacheva, M., J. Pares, N. Jordanova, and V. Karloukovski (1995), A new contribution to the archaeomagnetic study of a Roman pottery kiln from Calahorra (Spain), *Geophys. J. Int.*, *123*, 931–936.

Krása, D., C. Heunemann, R. Leonhardt, and N. Petersen (2003), Experimental procedure to detect multidomain remanence during Thellier-Thellier experiments, *Phys. Chem. Earth*, *28*, 681–687.

Leonhardt, R., C. Heunemann, and D. Krása (2004a), Analyzing absolute paleointensity determinations: Acceptance criteria and the software thelliertool4.0, *Geochem. Geophys. Geosyst.*, *5*, Q12016, doi:10.1029/2004GC000807.

Leonhardt, R., D. Krása, and R. S. Coe (2004b), Multidomain behavior during Thellier paleointensity experiments: A phenomenological model, *Phys. Earth Planet. Inter.*, *147*, 127–140.

Leonhardt, R., J. Matzka, A. Nichols, and D. Dingwell (2006), Cooling rate correction of paleointensity determination for volcanic glasses by relaxation geospeedometry, *Earth Planet. Sci. Lett.*, *243*, 282–292.

Leonhardt, R., K. Fabian, and E. Schnepp (2010), Holocene global geomagnetic field reconstruction based on archeomagnetic data: Assessing error sources and uncertainties, *Geophys. Res. Abstr.*, *12*, Abstract EGU2010-9421.

Marti, J., J. Mitjavila, and V. Arana (1994), Stratigraphy, structure and geochronology of Las Canadas Caldera (Tenerife, Canary Islands), *Geol. Mag.*, *131*(6), 715–727.

McClelland-Brown, E. (1984), Experiments on TRM intensity dependence on cooling rate, *Geophys. Res. Lett.*, *11*, 205–208.

Narayanaswamy, O. S. (1971), A model of structural relaxation in glass, *J. Am. Ceram. Soc.*, *54*, 491–498.

Narayanaswamy, O. S. (1988), Thermorheological simplicity in the glass transition, *J. Am. Ceram. Soc.*, *71*, 900–904.

Nichols, A., M. Potuzak, and D. Dingwell (2009), Cooling rates of basaltic hyaloclastites and pillow lava glasses from the HSDP2 drill core, *Geochim. Cosmochim. Acta*, *73*, 1052–1066.

Parés, J. M., R. De Jonge, J. O. Pascual, A. Bermúdez, and C. J. Tovar (1992), Archaeomagnetic evidence for the age of a Roman pottery kiln from Calahorra (Spain), *Geophys. J. Int.*, *112*, 533–537.

Pick, T., and L. Tauxe (1993), Geomagnetic paleointensities: Thellier experiments on submarine basaltic glass from the East Pacific Rise, *J. Geophys. Res.*, *98*, 17,949–17,964.

Potuzak, M., A. Nicholls, D. Dingwell, and D. Clague (2008), Hyperquenched basaltic glass from Loihi seamount, Hawaii, *Earth Planet. Sci. Lett.*, *270*, 54–62.

Riisager, P., and J. Riisager (2001), Detecting multidomain magnetic grains in Thellier paleointensity experiments, *Phys. Earth Planet. Inter.*, *125*, 111–117.

Selkin, P. A., and L. Tauxe (2000), Long-term variations in paleointensity, *Philos. Trans. R. Soc. London*, *358*, 1065–1088.

Smirnov, A. V., and J. A. Tarduno (2003), Magnetic hysteresis monitoring of Cretaceous submarine basaltic glass during Thellier paleointensity experiments: Evidence for alteration and attendant low field bias, *Earth Planet. Sci. Lett.*, *206*, 571–585.

Tauxe, L., T. A. T. Mullender, and T. Pick (1996), Potbellies, wasp-waists and superparamagnetism in magnetic hysteresis, Relation between inelastic deformability and thermal expansion of glass in its annealing range, *J. Geophys. Res.*, *101*, 571–583.

Tool, A. Q. (1946), Relation between inelastic deformability and thermal expansion of glass in its annealing range, *J. Am. Ceram. Soc.*, *29*, 240–253.

Veitch, R. J., I. G. Hedley, and J.-J. Wagner (1984), An investigation of the intensity of the geomagnetic field during Roman times using magnetically anisotropic bricks and tiles, *Arch. Sci. Geneve*, *37*, 359–373.

Wilding, M. C., S. L. Webb, and D. B. Dingwell (1995), Evaluation of a relaxation geospeedometer for volcanic glasses, *Chem. Geol.*, *125*, 137–148.

Wilding, M. C., S. L. Webb, D. B. Dingwell, G. Ablay, and J. Marti (1996a), Cooling variations in natural volcanic glasses from Tenerife, Canary Islands, *Contrib. Mineral. Petrol.*, *125*, 151–160.

Wilding, M. C., S. L. Webb, and D. B. Dingwell (1996b), Tektite cooling rates: Calorimeteric relaxation geospeedometry applied to natural glass, *Geochim. Cosmochim. Acta*, *60*, 1099–1103.

Wohlfarth, E. P. (1958), Relations between different modes of acquisition of the remanent magnetization of ferromagnetic particles, *J. Appl. Phys.*, *29*, 595–596.

D. B. Dingwell, K.-U. Hess, and F. W. von Aulock, Department of Earth and Environmental Sciences, Ludwig-Maximilians-Universität, D-80333 Munich, Germany.

A. Ferk and R. Leonhardt, Conrad Observatory, Central Institute for Meteorology and Geodynamics, A-1190 Vienna, Austria. (annika.ferk@geophysik.uni-muenchen.de)